Pro gradu -tutkielma

Teoreettinen fysiikka

The Effect of
Matter and Baryon Densities
on the
Cosmic Microwave Background Anisotropy

Reijo Keskitalo

2005

Ohjaaja: Dos. Hannu Kurki-Suonio

Tarkastajat: Dos. Hannu Kurki-Suonio, Prof. Kari Enqvist

HELSINGIN YLIOPISTO

FYSIKAALISTEN TIETEIDEN LAITOS

PL 64

00014 Helsingin yliopisto

Acknowledgments

Contents

List of Figures

Chapter 1

Introduction

Ever since its discovery[25] in 1965 the cosmic microwave background radiation (CMB) has been a subject of relentless efforts to reveal its origins and structure. Immediately, it was realized that the seemingly isotropic[1] black-body radiation must originate from the smooth primeval plasma[4] and can be traced back to the flaming youth of our universe. The photons we observe as CMB have scattered from ionized plasma when the universe was only $400\,000$ years old.

Although it was suggested on theoretical grounds that the CMB should exhibit the perturbed structure of the early universe, it was not until 1992 that the Cosmic Background Explorer (COBE) mission was able to measure the 10^{-5} order fluctuations in the nearly perfectly smooth radiation background of our sky[30]. Those fluctuations correspond to similar fluctuations in the matter that are the seeds which by now have grown to the complex structures we observe as galaxies, galaxy clusters and other large scale inhomogeneity.

After the COBE mission numerous attempts have been made to improve the precision at which the anisotropies of the CMB are known. To this day the most precise measurement was provided by the Wilkinson Microwave Anisotropy Probe[2] (WMAP) in 2003. The European Space Agency (ESA) is preparing the launch of its Planck[6] satellite in the year 2007. The comparison of the angular power spectrum of the observed CMB sky[10] with spectra that were derived from different theoretical models provides constraints on the cosmological parameters[31] that define different cosmological models. Examples of these parameters are the matter and baryon densities of our universe.

Study of the CMB as well as other observations of the masses of galaxies and galaxy clusters indicate the existence of a yet undiscovered form of matter. We can only observe it through its gravitation; it is completely transparent to electromagnetic radiation. On the account of this property, the missing matter component is called *dark matter*. It actually seems that dark matter is the dominant component of the matter density in our universe, there being roughly five times more dark than baryonic matter in terms of energy density[32]. Theories that treat the dark matter problem separate between hot dark matter (HDM) that consists of light, initially relativistic particles and cold dark matter (CDM) that is nonrelativistic in the early universe[3].

Analysis has shown that the way the primeval perturbations present themselves on the sky gives us detailed information about the content of our universe. In this thesis,

---

[1]That is, not dependent on direction.

we will explore some aspects of this analysis as we study the effect of cold dark matter and baryon densities on the formation of these anisotropies.

1.1   The Primeval Fireball

From redshift observations of distant galaxies, we know that the universe is expanding. The *Hubble law*, named after Edwin Hubble, the discoverer of the cosmic expansion, states that distant objects recede from us at a speed that is proportional to their distance[14]:

$$v = dH_0, \tag{1.1}$$

where v is the speed at which the object recedes, d is its distance and H_0 is the Hubble parameter value measured today. The Hubble parameter is often expressed equivalently as

$$H_0 \equiv h \cdot 100 \ \mathrm{km\,s^{-1}Mpc^{-1}}, \tag{1.2}$$

where h is now a new Hubble parameter.

If the universe is expanding, it is natural to assume that we could trace back its expansion into denser and denser settings in which the energy density of the universe would eventually exceed all limits achievable by particle accelerators. Already at much lower energies we would reach a temperature where the average energy of particles would not allow them to stay neutral. Matter would ionize, filling the universe with hot plasma, the primeval fireball.

Had this fireball been completely homogeneous, the following phases of the universe would have been somewhat uninteresting: expansion, rarefaction and cooling with only complete void as a limit. Of course this progress would not have lead to birth of observers to admire this inevitable slow fading into nothingness. However anyone of us can look into the night sky and observe that the universe is far from homogeneous. It has *structure*.

Cosmologically speaking anything less than a galaxy is beyond the resolution of our equations. Galaxies group up to clusters. The clusters arrange themselves into something beyond. These *large scale structures* have their seeds in the slight imperfections of the primeval fireball.

How the primordial inhomogeneities of the plasma came to be, is a matter of physics in extreme conditions. There exists compelling indications about a period of exponential, accelerating growth of the universe, *inflation*, when it was only a fraction of a second old[9]. It is believed that during this expansion, the quantum fluctuations of the scalar field that is responsible of the expansion, were extended beyond causal contact. The scales at which the perturbations were manifested *exited the horizon*.

After the exponential growth epoch, the expansion decelerates. The energy density of the universe is dominated by radiation whose gravity slows down the expansion. The perturbations that remain frozen beyond the horizon begin to enter the horizon and evolve deterministically by the physics of more comprehensible energies.

The evolution of these entering scales is determined by a set of cosmological parameters like the densities of baryons, neutrinos, dark matter and dark energy. All these parameters have their distinct imprint on the evolution of the perturbations.

As the expansion decreases the energy density, the plasma cools down. Eventually, electrons are able to bind themselves to nuclei. The plasma neutralizes, *recombination* occurs. Prior to this, the photons have rapidly scattered from the protons and (mainly)

electrons but are now freed by the recombination. It is these photons that we can observe, cooled down by the expansion along their way, as the cosmic microwave radiation. They carry with themselves a snapshot of the primeval fireball at recombination.

Making only some simple assumptions about the nature of the primordial perturbations we can study what kind of imprints different cosmic parameters should leave on the observed anisotropies of the CMB. Many of these effects are related to the acoustic oscillations of the coupled photon-baryon fluid. The ionized baryon[2] gas is kept in equilibrium with the photon gas through Thomson scattering to the extent, that their evolution can be described as a single, photon-baryon fluid until the coupling breaks in recombination, the neutralization of the plasma.

When the fluid density at some point is perturbed it creates a gravitational well that attracts both the photon-baryon fluid as well as dark matter into it. As the fluid is compressed, it heats up. The photon pressure rises with the temperature which eventually reverses the contraction. The fluid begins to rarefy driven by the photon pressure. If the energy density of the universe is still dominated by radiation, the gravitational well becomes more shallow. However dark matter does not interact with the photons and keeps contracting into the well. The reversing pressure gradient with the aid of gravitation end inevitably the rarefaction of the photon-baryon fluid which compresses again. This motion is called the acoustic oscillation.

The dynamics of the photon-baryon fluid are fascinating. Their interaction through Thomson scattering leads to a single fluid system with a component that has inertia, and another one without it. The baryons *drag* the oscillations with their weight. The photon component adds another effect: they carry energy over the perturbations and smoothen out the gravitational perturbations in the radiation dominated universe.

Cold dark matter begins its role as a mere bystander and is forced to follow the gravitational pull of the photon overdensities. Since this process is set up in the frame of an expanding universe, the roles eventually change. The energy density of the dark matter exceeds the energy density of radiation and begins to dominate the formation of structure in the universe.

We will addresses two complex questions: how does the dynamical behavior of the primeval plasma change as matter and baryon densities change and how are these effects observed in the anisotropies of the CMB? Tools of this process include both analytical as well as computational methods though the emphasis is on the computational approach.

1.2 Conventions

A Greek letter $\alpha, \beta, \ldots$ as an index is understood be assigned values from 0 to 3, and Latin letters $i, j, \ldots$ get values from 1 to 3, referring to the spatial parts of the quantities in question. We will also assume the Einstein summation convention, where applicable. Furthermore, we will employ subindex zero when denoting present day value, for instance in H_0.

In this thesis we will use the metric signature $\{-, +, +, +\}$ and operate in the conformal Newtonian gauge[5, 17], also known as the longitudinal or zero shear gauge.

We assume a flat background universe. That is, a homogeneous universe with just

---

[2]For cosmologists baryons are the matter component that interacts with photons, unlike dark matter. Thus in addition to particles consisting of quarks, the term *baryon* refers also to electrons that are actually leptons.

the energy density to keep expanding forever. Models with more energy are referred as closed and models that have less energy are open. The expansion of the universe is computed from the flat, homogeneous background model. Furthermore we will assume small perturbations about this homogeneous background and write evolution equations for these perturbations. Full perturbed values are then given as a sum of the background value and the perturbation. For instance the energy density:

$$\rho = \bar{\rho} + \delta\rho, \tag{1.3}$$

where the overbar denotes the background values and the δ denotes the perturbation parts.

The perturbed FRW metric is described as

$$g_{\mu\nu} = a^2(\eta_{\mu\nu} + h_{\mu\nu}), \tag{1.4}$$

where $\eta_{\mu\nu}$ is the flat Minkowski metric and $h_{\mu\nu}$ is the perturbation part. Divide it into components:

$$h_{\mu\nu} \equiv \begin{bmatrix} -2A & -B_i \\ -B_i & -2D\delta_{ij} + 2E_{ij} \end{bmatrix}. \tag{1.5}$$

Now the conformal Newtonian gauge assumes the perturbations to be of the scalar type and is defined by setting the B and E parts of this general form perturbation to zero. This yields us the metric perturbation in terms of two scalar perturbations A and D. We choose to denote them as Φ and Ψ respectively. Thus the line element for the perturbed metric reads (in terms of the conformal time, η):

$$\mathrm{d}s^2 = a^2(\eta)\left[-(1+2\Phi)\mathrm{d}\eta^2 + (1-2\Psi)\delta_{ij}\mathrm{d}x^i\mathrm{d}x^j\right] \tag{1.6}$$

Where it is not explicitly noted otherwise, we use as a time coordinate the conformal time, which is related to ordinary cosmic time by

$$\mathrm{d}\eta = \frac{\mathrm{d}t}{a(t)}, \qquad \eta = \int^t \frac{\mathrm{d}t'}{a(t')}, \tag{1.7}$$

where a is the scale factor, normalized to unity today, $a_0 = 1$. The conformal time gives the maximum coordinate distance light could have traveled since the Big Bang. That is, the size of causally connected regions.

Being a monotonic function of time, the scale factor provides another convenient way of dating events. Often in cosmology time is measured also as *cosmological redshifts*, z. It has little to do with the Doppler effect, even though both can be observed as the shifting of absorption lines. Cosmological redshift occurs because the universe expands as the light propagates. The scale factor and the redshift scales are related as

$$a = \frac{1}{1+z} \tag{1.8}$$

The scalar potentials of our gauge of choice are related to the gauge-invariant potentials of Bardeen[1], as

$$\Phi = \Phi_A \quad \Psi = -\Phi_H \tag{1.9}$$

When discussing the energy density of a given species of energy, its value is given relative to the critical energy density ρ_{crit}, the energy density of a flat universe. That is,

$$\Omega_i = \frac{\rho_i}{\rho_{\mathrm{crit}}} \quad \text{with} \quad \rho_{\mathrm{crit}} \equiv \frac{3H^2}{8\pi G}. \tag{1.10}$$

Here H is the Hubble parameter

$$H = \frac{1}{a}\frac{\mathrm{d}a}{\mathrm{d}t} \tag{1.11}$$

and G is the gravitational constant. These densities are parameters of the model. They evolve with time, so it is reasonable to define them in a fixed instant, namely present. Thus $\Omega_i \equiv \rho_{i0}/\rho_{\mathrm{crit}}$.

We will also encounter the *comoving Hubble parameter*:

$$\mathcal{H} = \frac{1}{a}\frac{\mathrm{d}a}{\mathrm{d}\eta} = \frac{1}{a}\left(a\frac{\mathrm{d}a}{\mathrm{d}t}\right) = \frac{\mathrm{d}a}{\mathrm{d}t} = aH \tag{1.12}$$

and the equation-of-state parameter

$$w = \frac{p}{\rho} \tag{1.13}$$

Magnitudes of the perturbations are given relative to the background values e.g. for the energy density of a given species i, we write

$$\delta_i \equiv \frac{\delta\rho_i}{\bar{\rho}_i}. \tag{1.14}$$

For velocity perturbations there is no background velocity since the Newtonian gauge is chosen so that the fluid is at rest in the comoving coordinates. Thus

$$v_i \equiv \delta v_i \tag{1.15}$$

In our calculations we will employ the *natural unit system $k_B = c = \hbar = 1$* and where applicable we will scale dimensional variables with the present Hubble parameter H_0 or if the Hubble parameter depends on the variables we study, H_{100}. These are related as:

$$H_0 \equiv h \cdot 100\,\mathrm{km\,s}^{-1}\mathrm{Mpc}^{-1} \equiv h \cdot H_{100} \approx \frac{h}{3000\,\mathrm{Mpc}} \approx \frac{h}{9.78\,\mathrm{Ga}}, \tag{1.16}$$

where "Ga" stands for 10^9 years. For the remainder of this work, h is understood to refer to the Hubble parameter. A typical value used in this work is $h = 0.5$. Observations prefer a somewhat higher value[31]: $h = 0.72 \pm 0.05$. This apparent discrepancy is explained by our parametrization in Section 2.1.

Chapter 2

Method

The basic tool for describing inhomogeneities in the standard cosmological model is the linear perturbation theory[5, 17] (for a detailed treatment see ref. [22] and the references therein). In it the universe is described as flat and homogeneous and upon this background, small Gaussian perturbations are introduced.

In the Einsteinian universe the laws of physics are formulated in terms of tensor quantities. The perturbations can be understood as tensor fields in the background spacetime. However these fields depend on the gauge chosen. The perturbations can be separated into scalar, vector and tensor perturbations which can be studied independently in linear perturbation theory. Vector perturbations decay in an expanding universe and tensor perturbations generate gravitational waves, that do not couple to energy density inhomogeneities[22]. In this research the chosen gauge, the Newtonian gauge, assumes scalar perturbations[21].

The set of scalar perturbations relevant to our model of the universe is given in Table 2.1.

Φ	The gravitational perturbation, as given in (1.6)
Θ_ℓ	Multipoles of the angular expansion of photon temperature anisotropy
δ_c	Relative energy density perturbation for cold dark matter
v_c	Dark matter velocity perturbation
δ_b	Relative energy density perturbation for baryon fluid
v_b	Baryon fluid velocity perturbation

Table 2.1: The scalar perturbations relevant for our model.

The photon temperature anisotropies deserve a few lines. Let us denote the perturbed distribution function for the photons by

$$f(\eta, \mathbf{x}, \mathbf{p}) = \frac{1}{\exp\left(\frac{p}{\bar{T}(\eta)(1+\Theta(\eta,\mathbf{x},\mathbf{p}))}\right) - 1},$$ (2.1)

where the background photon temperature is $\bar{T}(\eta)$ and local perturbations to this temperature are denoted by Θ, the *brightness function*. The perturbed temperature is thus

$$T(\eta, \mathbf{x}, \mathbf{p}) = \bar{T}(\eta)(1 + \Theta(\eta, \mathbf{x}, \mathbf{p})), \tag{2.2}$$

The brightness function is related to the photon distribution function. The distribution in the background universe is the *Bose-Einstein* distribution: $f(\eta, \mathbf{x}, \mathbf{p}) = 1/\left(e^{(E-\mu)/T} - 1\right)$ with $\mu = 0$. The photon chemical potential is zero since there is no photon number conservation.

Here $\mathbf{p}$ is the momentum of the cosmic fluid. Its magnitude has a second order effect on the brightness function[20] and is thus negligible, therefore $\Theta = \Theta(\eta, \mathbf{x}, \hat{\mathbf{p}})$.

The first photon multipoles can now be defined using $\hat{\mathbf{p}}$:

$$\Theta_0 = \frac{1}{4\pi} \int \Theta(\hat{\mathbf{p}}) \mathrm{d}\Omega \tag{2.3}$$

$$\overrightarrow{\Theta_1} = \frac{1}{4\pi} \int \hat{\mathbf{p}} \Theta(\hat{\mathbf{p}}) \mathrm{d}\Omega \tag{2.4}$$

$$\Theta_2^{ij} = \frac{1}{4\pi} \int (\hat{\mathbf{p}}^i \hat{\mathbf{p}}^j + \frac{1}{3} \delta^{ij}) \Theta(\hat{\mathbf{p}}) \mathrm{d}\Omega. \tag{2.5}$$

We assume scalar perturbations and thus relate the vector and tensor quantities to scalar source terms:

$$\overrightarrow{\Theta_1} \equiv -\nabla \Theta_1 \tag{2.6}$$

$$\Theta_2^{ij} \equiv (\partial_i \partial_j - \frac{1}{3} \delta_{ij} \nabla^2) \Theta_2 \tag{2.7}$$

2.1 The Model of the Universe

To define the background on which the perturbations evolve we need a simplified model of the universe. Since the observations clearly favor a flat or close to flat solution, we set the energy density of the universe equal to the critical density i.e., $\Omega = 1$. Because this thesis focuses on the effect of baryon and CDM content to the structure formation, we ignore the effect of dark energy. The results of discarding the dark energy will be discussed in more detail with the angular power spectrum. Thus our universe is made up of radiation, baryonic matter (nucleons and electrons) and cold dark matter:

$$\Omega = 1 = \Omega_\gamma + \Omega_b + \Omega_c. \tag{2.8}$$

Of these, the photon energy density parameter is fixed by the CMB temperature, T_0. The density parameters manifest in the equations as *physical density parameters*: $\omega_i = \Omega_i h^2$ We choose to parametrize our model by the physical matter and baryon density parameters, $\omega_m \equiv \omega_c + \omega_b$ and ω_b, respectively.

Photon density parameter is negligible at present (of order $\sim 10^{-5}$). Observations indicate that a good deal of the universe's energy density is due to dark energy ($\Omega_\Lambda \approx 0.70$), but we set $\Omega_\Lambda = 0$ leaving matter density parameter close to unity: $\Omega_m \approx 1$. This modification has little effect on the physics of the CMB, since dark energy density if significant only in the late universe.

Recent observations[31] indicate that $\omega_m = 0.14 \pm 0.02$. Thus we need to reduce the value of Hubble parameter h in order to conform our model with the observed physical matter density. For $\omega_m = 0.20$ (the reference model value) we have $h \approx 0.447$.

The model parameters set values for two important background quantities, the instant of matter-radiation-equality a_{eq} and the baryon-photon-momentum-ratio, R. Since $\rho_r \propto a^{-4}$ and $\rho_m \propto a^{-3}$, we can trace these densities back to the equality:

$$\rho_{r0} a_{\text{eq}}^{-4} = \rho_{m0} a_{\text{eq}}^{-3} \quad \Rightarrow \quad a_{\text{eq}} = \frac{\rho_{r0}}{\rho_{m0}} = \frac{\frac{\pi^2}{30} \left[2 + \frac{21}{4} \left(\frac{4}{11}\right)^{4/3}\right] T_0^4}{\Omega_m \rho_{\text{crit}}} \tag{2.9}$$

$$a_{\text{eq}} = \frac{\pi^3 G}{45 H_{100}^2} \left[8 + 21 \left(\frac{4}{11}\right)^{4/3}\right] \frac{T_0^4}{\omega_m}, \tag{2.10}$$

where the expression for $\rho_r(T)$ includes neutrino contribution and follows from integration of the background distribution function. The baryon-photon-momentum-ratio is

$$R = \frac{\rho_b + p_b}{\rho_\gamma + p_\gamma} \approx \frac{\rho_b}{\rho_\gamma + \frac{1}{3}\rho_\gamma} = \frac{3\rho_b}{4\rho_\gamma} = \frac{3\rho_{b0} a^{-3}}{4\rho_{\gamma0} a^{-4}} \stackrel{(2.9)}{=} \frac{3\Omega_b \rho_{\text{crit}} a}{4\frac{\pi^2}{15} T_0^4} = \frac{135 H_{100}^2}{32\pi^3 G T_0^4} a\omega_b \tag{2.11}$$

In our model we approximate the baryonic matter by hydrogen and have no other elements.

The evolution mechanisms are described by the Einstein equation:

$$G_{\mu\nu} = 8\pi G T_{\mu\nu}, \tag{2.12}$$

where $G_{\mu\nu}$ is the Einstein tensor and $T_{\mu\nu}$ the energy-momentum tensor. The energy continuity equation $T^{\mu\nu}{}_{;\nu} = 0$ follows from the Einstein equation. Here $;\nu$ denotes covariant derivative. For an ideal fluid in its rest frame the tensor has the form $T_{\mu\nu} = \text{diag}(\rho, p, p, p)$

Finally the Boltzmann equation describes the evolution of the distribution function:

$$\frac{\text{d}f}{\text{d}t} \equiv \frac{\partial f}{\partial t} + \frac{\partial f}{\partial x^i}\frac{\text{d}x^i}{\text{d}t} + \frac{\partial f}{\partial p^i}\frac{\text{d}p^i}{\text{d}t} = \text{collision effects} \tag{2.13}$$

A detailed derivation of the set of equations governing the evolution of perturbations is given (for example) in [5, 16]. The resulting equations are

$$\Theta' + \hat{\mathbf{p}} \cdot \nabla\Theta + \hat{\mathbf{p}} \cdot \nabla\Phi - \Psi' = -\tau' \left[\Theta_0 - \Theta + \hat{\mathbf{p}} \cdot \mathbf{v}_b + \frac{3}{4}\hat{p}^i\hat{p}^j\Theta_2^{ij}\right] \tag{2.14}$$

$$\delta_c' + \nabla \cdot \mathbf{v}_c - 3\Psi' = 0 \tag{2.15}$$

$$\mathbf{v}_c' + \mathcal{H}\mathbf{v}_c + \nabla\Phi = 0 \tag{2.16}$$

$$\delta_b' + \nabla \cdot \mathbf{v}_b - 3\Psi' = 0 \tag{2.17}$$

$$\mathbf{v}_b' + \mathcal{H}\mathbf{v}_b + \nabla\Phi = -\tau'\frac{4\rho_\gamma}{3\rho_b}(\mathbf{v}_\gamma - \mathbf{v}_b), \quad \mathbf{v}_\gamma = 3\overrightarrow{\Theta}_1 \tag{2.18}$$

An important background parameter is also introduced here: the optical depth, $\tau(\eta)$, gives the amount of collisions a single photon experiences on average during the interval $[\eta, \eta_0]$. It is defined as

$$\tau(\eta) = \int_\eta^{\eta_0} \text{d}\eta \, a n_e \sigma_T \tag{2.19}$$

where n_e is the electron number density and σ_T is the cross section for Thomson scattering. From the definition it is obvious that $\tau(\eta_0) = 0$. Quite naturally its derivative is the collision rate:

$$\tau'(\eta) = -a n_e \sigma_T \tag{2.20}$$

For many background quantities the scale factor, a, plays a significant role. In our simplified case the Friedmann equation:

$$\mathcal{H}^2 = \left(\frac{1}{a}\frac{\mathrm{d}a}{\mathrm{d}\eta}\right) = \frac{8\pi G}{3}\rho a^2 \tag{2.21}$$

provides the means to solve for $a(\eta)$ in a universe that is co-dominated by matter and radiation. The solution[22] is

$$a(\eta) = \frac{\eta}{\eta_3}\left(2 + \frac{\eta}{\eta_3}\right)a_{\mathrm{eq}}, \tag{2.22}$$

where η_3 is a shorthand notation[1] for $\eta_3 \equiv \eta_{\mathrm{eq}}/(\sqrt{2}-1)$. Here as well as anywhere else the subscript "eq" refers to the value during matter-radiation equality. That is, the moment when the two components have equal energy densities.

Solving $a(\eta)$ enables us to write

$$\mathcal{H} = \frac{a'}{a} = \frac{\eta_3 + \eta}{\eta\eta_3 + \frac{1}{2}\eta^2} \tag{2.23}$$

We still need two equations for the gravitational perturbations. Here we make an important approximation. The difference of the two potentials, Φ and Ψ, is related to the deviations from the perfect fluid form of the energy tensor[5]. This is only relevant before matter domination since the energy tensor of non-relativistic matter (dust) has the perfect fluid form. We extend the perfect fluid approximation to cover the radiation dominated epoch and write

$$\Phi = \Psi. \tag{2.24}$$

Thus we only need one equation for the gravitational potential. It is the first order correction to the Friedmann equation:

$$\nabla^2\Phi - 3\mathcal{H}(\Psi' + \mathcal{H}\Phi) = 4\pi Ga^2\delta\rho \tag{2.25}$$

Primordial perturbations in the smooth photon-matter content of the universe extend to a large range of scales due to inflation. In linear perturbation theory, the evolution of an individual scale of perturbations is independent of other scales. This enables us to Fourier transform the set of differential equations that describe the evolution of the perturbations to separate out the evolution of a single scale, parametrized by the Fourier mode, k.

Fourier transforming the scalar velocity perturbation, $\mathbf{v} = \nabla v$, as[20]:

$$v(\mathbf{x}) = \int v(\mathbf{k})e^{i\mathbf{k}\cdot\mathbf{x}}\frac{\mathrm{d}k}{k} \tag{2.26}$$

giving

$$\mathbf{v_k} = -i\hat{\mathbf{k}}v \tag{2.27}$$

and expanding the angular dependent parts in terms of Legendre polynomials,

$$f(\cos\theta) = \sum_{\ell=0}^{\infty}(-i)^{\ell}(2\ell+1)f_{\ell}P_{\ell}(\cos\theta), \tag{2.28}$$

---

[1]In ref. [22] η_3 is denoted by η_{eq}.

where

$$f_\ell = i^\ell \int_{-1}^{1} \frac{\mathrm{d}\cos\theta}{2} P_\ell(\cos\theta) f(\cos\theta), \tag{2.29}$$

the set of partial differential equations (2.14)-(2.18) and (2.25) can be cast into the form[5, 21]:

$$-k^2\Phi - 3\mathcal{H}(\Phi' + \mathcal{H}\Phi) = 4\pi G a^2(\rho_c\delta_c + \rho_b\delta_b + 4\rho_\gamma\Theta_0) \tag{2.30}$$

$$\Theta_0' + k\Theta_1 - \Phi' = 0 \tag{2.31}$$

$$\Theta_1' + \frac{k}{3}(2\Theta_2 - \Theta_0) - \frac{k}{3}\Phi = -\tau'(\frac{1}{3}v_b - \Theta_1) \tag{2.32}$$

$$\Theta_2' + \frac{k}{5}(3\Theta_3 - 2\Theta_1) = -\tau'\left[\frac{1}{10}(\Theta_2 + \Theta_0^p + \Theta_2^p) - \Theta_2\right] \tag{2.33}$$

$$\Theta_\ell' + \frac{k}{2\ell+1}\left[(\ell+1)\Theta_{\ell+1} - \ell\Theta_{\ell-1}\right] = \tau'\Theta_\ell, \quad \ell \geq 3 \tag{2.34}$$

$$\delta_c' + kv_c - 3\Phi' = 0 \tag{2.35}$$

$$v_c' + \mathcal{H}v_c - k\Phi = 0 \tag{2.36}$$

$$\delta_b' + kv_b - 3\Phi' = 0 \tag{2.37}$$

$$v_b' + \mathcal{H}v_b - k\Phi = -\tau'\frac{4\rho_\gamma}{3\rho_b}(3\Theta_1 - v_b). \tag{2.38}$$

The manner in which the lower multipoles depend on the higher multipoles is referred to as the *Boltzmann hierarchy*. The multipoles with the upper index p in the quadrupole equation correspond to a similar hierarchy in the photon polarization.

Even though the lowest photon multipoles, the monopole Θ_0 and the dipole Θ_1 enter here simply as the first terms of the Fourier transformed Legendre expansion of the brightness function, they have a specific physical significance. Integrating the perturbed distribution function (2.1) one finds that

$$\delta_\gamma = \frac{\delta\rho_\gamma}{\bar{\rho}_\gamma} = 4\Theta_0 \tag{2.39}$$

$$v_\gamma = 3\Theta_1 \tag{2.40}$$

valid in both real and Fourier space.

2.2   The Angular Power Spectrum

The perturbations of the preceding section are responsible for the anisotropy of the CMB. The quantitative analysis of the observed anisotropies is based on the angular power spectrum that tells us the magnitudes at which different angular scales of perturbations are exhibited. First, take the CMB temperature anisotropy to be a function over the celestial sphere

$$\Theta(\theta, \phi) \equiv \frac{\delta T}{T_0}(\theta, \phi). \tag{2.41}$$

It is related to our brightness function as

$$\Theta(\theta, \phi) = \Theta(\eta = \eta_0, \mathbf{x} = 0, -\hat{\mathbf{p}}), \tag{2.42}$$

where $\hat{\mathbf{p}}$ is the unit vector pointing in the direction (θ, ϕ)).

Expand now the anisotropy in terms of the spherical harmonics

$$\Theta(\theta,\phi) = \sum a_{\ell m} Y_{\ell m}(\theta,\phi), \qquad a_{\ell m} = \int Y_{\ell m}^* \Theta d\Omega. \tag{2.43}$$

Now we may define the angular power spectrum as

$$C_\ell \equiv \langle |a_{\ell m}|^2 \rangle = \frac{1}{2\ell+1} \sum_{|m| \le \ell} \langle |a_{\ell m}|^2 \rangle \tag{2.44}$$

which nicely exhibits that we only consider the angular scale, depending on ℓ, not the orientation through m.

The first generation of programs that computed the angular power spectrum used the full set of equations (2.30)-(2.38). The necessary number of multipole equations according to (2.34) were added to reach the desired angular scale. Truncation errors that propagate to lower multipoles through the Boltzmann hierarchy required the use of several more multipoles than the required angular scale, yet adding to the set of necessary equations. Ma and Bertschinger[21] report on using as much as 2000 multipoles.

However, shortly after their research, Seljak and Zaldarriaga[27], published a paper in 1996 describing a method to compute the higher multipoles from only a few of the lower multipoles. The method is known as the *line-of-sight integration* and it is the cornerstone of modern power spectrum computing programs such as the widely used *CMBFast* code[28]. All the multipoles we observe in the CMB have evolved from just a few of the lowest multipoles at decoupling, after which the photons free-stream to us. To follow their path one needs to integrate equation (2.14).

In this method the multipoles are computed in terms of a source function, $S(\eta, \mathbf{k})$, as follows:

$$\Theta_\ell(\eta_0, \mathbf{k}) = \int_0^{\eta_0} d\eta S(\eta, \mathbf{k}) j_\ell[k(\eta_0 - \eta)], \tag{2.45}$$

where j_ℓ are the spherical Bessel functions and the source term is

$$S(\eta, \mathbf{k}) = g(\Theta_0 + \frac{v_b'}{k} + \Phi + \frac{1}{4}\tilde{\Theta}_2 + \frac{3}{4k^2}\tilde{\Theta}_2'')$$
$$+ g'(\frac{v_b}{k} + \frac{3}{2k^2}\tilde{\Theta}_2') + g''(\frac{3}{4k^2}\tilde{\Theta}_2) + e^{-\tau}(\Phi' + \Psi'). \tag{2.46}$$

The form (2.45)-(2.46) results from the integration of Eq. (2.14) with the help of two partial integrations, and dropping the boundary terms which affect only $\Theta_0(\eta_0, \mathbf{k})$ and $\Theta_1(\eta_0, \mathbf{k})$ of which we are not interested.

Here $g(\eta)$ is the *visibility function*, defined as

$$g(\eta) \equiv -\tau' e^{-\tau}. \tag{2.47}$$

It can be understood to give the distribution of last scattering instances for the CMB photons. Also $\tilde{\Theta}_2$ is the quadrupole moment with corrections done to take into account the effect of polarization,

$$\tilde{\Theta}_2 = \Theta_2 + \Theta_0^P + \Theta_2^P \tag{2.48}$$

Using photon multipoles only up to $\ell = 8$ in the Boltzmann hierarchy and a truncation scheme introduced in [21], Seljak and Zaldarriaga were able to compute the spectrum with an accuracy better than 0.1%

We make a number of approximations to the method presented here. Most importantly we reduce the number of multipoles in our computations to two: Θ_0 and Θ_1. Correspondingly we neglect polarization as it is related to the evolution of the quadrupole moment (cf. equation (2.33)).

Secondly, for the purposes of line-of-sight integration, we replace v_b by $v_\gamma = 3\Theta_1$. As long as the photons and baryons remain tightly coupled, this is a very good approximation, since the photon-baryon fluid moves with only one velocity. During decoupling this relationship breaks, but it still takes time for the velocity perturbations to evolve away from each other.

Third, we apply a delta function approximation to the visibility function in (2.45), since it is sharply peaked near decoupling. For our purposes even this is justified and simplifies the calculations greatly. This ignores the effect of reionization[2] so we also omit it from our model. The visibility function is explored further in Figure 3.5.

Applying all these simplifications to (2.45) yields us a formula for an arbitrary multipole moment today:

$$
\begin{aligned}
\Theta_\ell(\eta_0, \mathbf{k}) = {} & [\Theta_0(\eta_{\mathrm{dec}}) + \Phi(\eta_{\mathrm{dec}})]j_\ell[k(\eta_0 - \eta_{\mathrm{dec}})] \\
& + 3\Theta_1(\eta_{\mathrm{dec}})j_\ell'[k(\eta_0 - \eta_{\mathrm{dec}})] \\
& + 2\int_0^{\eta_0} e^{-\tau}\Phi'(\eta)j_\ell[k(\eta_0 - \eta)]d\eta,
\end{aligned}
\tag{2.49}
$$

where we have used

$$
j_\ell'(x) = j_{\ell-1}(x) - \frac{\ell + 1}{x}j_\ell(x)
\tag{2.50}
$$

The first term in (2.49), $\Theta_0 + \Phi$, is known as the effective temperature perturbation. The lowest photon multipole, the monopole Θ_0 is directly proportional to the energy density perturbation of the photon gas and thus represents the temperature of the gas. Adding the gravitational perturbation Φ to it takes into account the redshift effects that the CMB photons experience due to different gravitational potentials at their origin. This effect is known as the ordinary Sachs-Wolfe effect (SW).

The second term, Θ_1, is the photon dipole and it is proportional to the photon gas velocity perturbation. Its significance is promoted by the fact that the baryon collisions manifest first in this term of the Boltzmann hierarchy.

The last term describes the redshift effects the photons undergo after the last scattering. During their travel they cross over evolving potential wells. If the depth of the well changes during the passing, there is a net redshift effect that changes the temperature of the photon. This phenomenon is referred to as the integrated Sachs-Wolfe effect (ISW).

We have now the Fourier transformation for the photon temperature anisotropy. To compute the angular power spectrum in *real* space we need to inverse Fourier transform it and then compute its spherical harmonic expansion. By applying an adiabatic perturbation approximation[3] and conducting the transformation one reaches

$$
C_\ell = 4\pi \int_0^\infty \frac{\mathrm{d}k}{k} \mathcal{P}_{\mathcal{R}}(\mathbf{k}) T_{\mathcal{R}\ell}(k)^2,
\tag{2.51}
$$

---

[2]The CMB originates from the neutralization of the cosmic plasma, when the content of the universe becomes transparent. The interstellar gas is again ionized by the formation of stars, but the universe remains transparent due to decreased density.

[3]The adiabatic approximation is well supported by recent analysis of CMB observations[33].

where $\mathcal{P}_{\mathcal{R}}$ is the power spectrum of the primordial curvature perturbation $\mathcal{R}$. The curvature perturbation is related to the three dimensional scalar curvature of the constant time slices that remain constant for scales that are outside horizon in the comoving gauge. In the adiabatic approximation all other perturbations can be defined using the curvature perturbation, as will be discussed in Section 2.4.

$T_{\mathcal{R}\ell}$ is the transfer function defined as $\Theta_\ell(\mathbf{k}, \eta_0) \equiv \mathcal{R}(\mathbf{k})T_{\mathcal{R}\ell}(k)$, i.e. the transfer function describes how the primordial curvature perturbation evolves into present day CMB temperature perturbations. For our computations we set the initial curvature perturbation to $\mathcal{R} = 1$. This means that (2.49) defines the transfer function.

Simplest inflationary models produce nearly scale-invariant perturbations, for which the power spectrum of the initial values (the primordial power spectrum) can be approximated by a power law:

$$\mathcal{P}_{\mathcal{R}}(k) = A^2 \left(\frac{k}{k_p}\right)^{n-1} , \tag{2.52}$$

where the amplitude A and the spectral index $n \approx 1$ are constants and k_p is a reference scale called the pivot scale. We approximate $n = 1$, eliminating k_p.

For our calculations we may set $A = 1$ later to be rescaled to agree with data. These approximations leave us with

$$C_\ell = 4\pi \int_0^\infty \frac{\mathrm{d}k}{k} \Theta_\ell^2(\eta_0, k). \tag{2.53}$$

Equation (2.53) along with (2.49) plays a central role in the computation.

2.2.1 Silk Damping

Because of our abrupt truncation of the Boltzmann hierarchy, no explicit damping takes place in the time evolution of the perturbations. However we know, that for small scales (large k), the oscillations of the anisotropies are significantly diminished by radiation diffusion[29] which our approximation neglects. In the oscillating photon-baryon fluid the photons conduct random walks carrying energy from the hot regions to colder ones. Since the pressure which drives the oscillations is proportional to the temperature, this damps the oscillations. Dodelson presents in his book[5] a method to include the damping effect into the angular power spectrum in an approximate manner, without resorting to the integration of several photon multipoles in order to model the effect. The solution approximates tight coupling to apply, scale to be small (well within the horizon, $k\eta \ll 1$) and the remaining gravitational perturbation negligible. In this setting the inclusion of the photon quadrupole equation yields the damping scale, though through some cumbersome calculations.

The damping scale, k_D, is included in the calculation by multiplying the oscillating quantities, Θ_0 and Θ_1, by a *damping function*:

$$D(\eta) \equiv e^{-k^2/k_D^2(\eta)} \tag{2.54}$$

For k_D, we find[4]

$$\frac{1}{k_D^2(\eta)} = \int_0^\eta \frac{\mathrm{d}\eta'}{6(1+R)n_e\sigma_T a(\eta')} \left[\frac{R^2}{1+R} + \frac{8}{9}\right], \tag{2.55}$$

---

[4]The formula presented here does not take into account the effect of polarization. To include polarization[16], replace the numeric constant 8/9 by 16/15.

where $R \propto \omega_b a$.

For a qualitative discussion let us write the electron density as $n_e = const \cdot \omega_b \cdot a^{-3}$ and consider two cases: radiation ($a \propto \eta$) and matter domination ($a \propto \eta^2$). It can be computed, that even for high baryon densities, R is of the order of unity at decoupling. During matter domination $R \propto \omega_b \eta^2$, so it is reasonable to approximate its effect on the integral negligible for an order-of-magnitude estimate. These actions provide us with

$$\frac{1}{k_D^2(\eta)} \overset{\text{rad.dom.}}{\propto} \frac{\eta^3}{\omega_b} \quad \text{and} \quad \frac{1}{k_D^2(\eta)} \overset{\text{mat.dom.}}{\propto} \frac{\eta^5}{\omega_b}, \tag{2.56}$$

that is, the damping extends to larger scales faster during matter domination. It translates into two qualitative predictions about diffusion damping: earlier matter-radiation equality implies smaller k_D and thus stronger damping effects. Higher baryon densities spell larger k_D; baryons inhibit diffusion damping. The latter is somewhat unsurprising, since the photon mean free path is dictated by the electron density and thus by baryon density.

The damping function is a rapidly decreasing function near recombination and thus the delta function approximation performed on the visibility function does it no justice. To take into account for this effect we replace

$$e^{-k^2/k_D^2(\eta_{\text{dec}})} \quad \text{by} \quad \int_0^{\eta_0} \mathrm{d}\eta \; g(\eta) e^{-k^2/k_D^2(\eta)} \tag{2.57}$$

after applying the delta function approximation in (2.45). The difference of this abrupt damping scheme and the integral approach can be viewed from Figure 2.1.

2.2.2   Recombination

When the universe has cooled down to approximately 4000 degrees Kelvin, ionized hydrogen recombines rapidly. In the process the until-now-opaque content of the universe becomes transparent. The optical depth decreases by many orders of magnitude from, $\tau \gg 1$ to $\tau \ll 1$ (see Fig. 2.2, lower half).

Recombination is the most significant epoch from which the visibility function receives its contribution. In more detailed models reionization inflicts another visible peak. We choose not to model reionization in this order of the calculations.

The key variable in recombination is the ionization fraction, x. If our model included helium, its ionization would need to be described with a different ionization fraction. We define x to be the fraction of free electrons with respect to all electrons. Since the universe is electrically neutral, the latter is equal to the number of protons. Thus

$$x = \frac{n_e}{n_e^*} = \frac{n_e}{n_p^*}, \tag{2.58}$$

where the number of free electrons is n_e and the total number of electrons or protons are denoted with the asterisk.

We will require both the electron and photon number densities. Photon number can be computed as a function of temperature by integrating the photon distribution function. Approximating all baryons as nonrelativistic hydrogen nuclei (protons) we may compute hydrogen number density simply by dividing baryon energy density by proton mass. Thus

$$n_\gamma = \frac{2}{\pi^2}\zeta(3)T^3 \quad \text{and} \quad n_p^* \approx n_B \approx n_{e^*} \approx \frac{\rho_b}{m_p} = \frac{\rho_{b0}a^{-3}}{m_p} = \frac{\Omega_b \rho_{\text{crit}}}{m_p a^3} \tag{2.59}$$
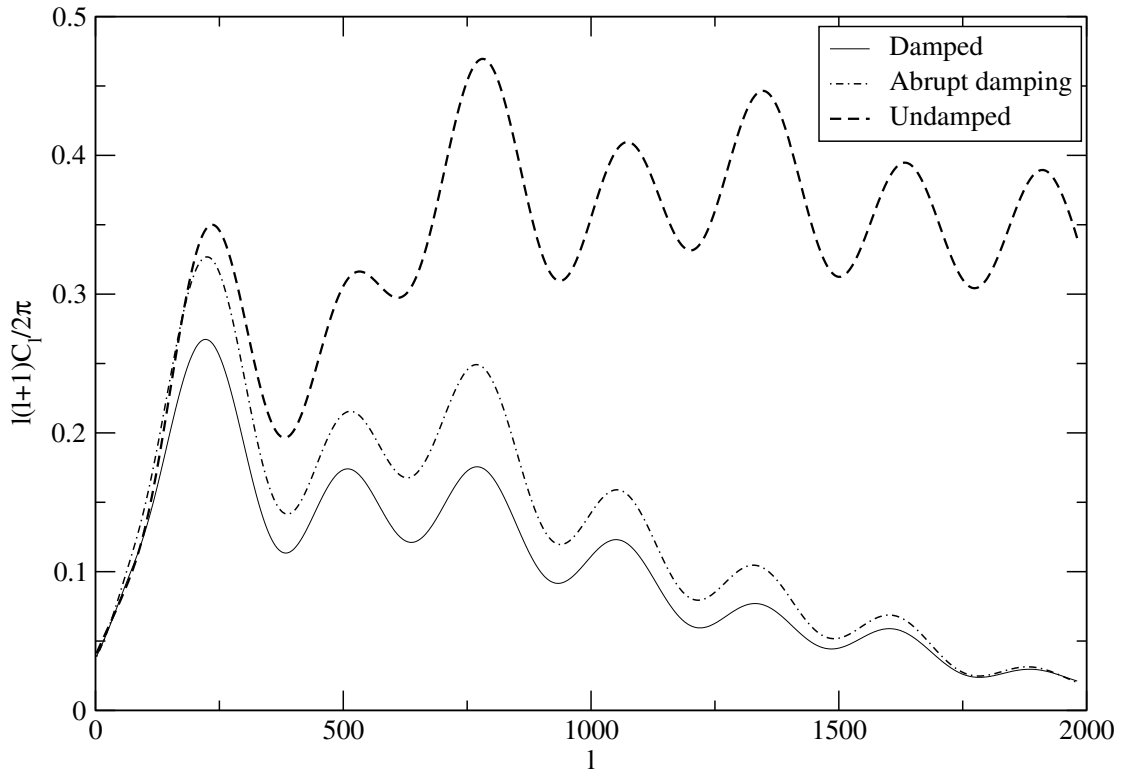
Figure 2.1:   An example power spectrum computed with and without the effects of damping. In the abrupt damping approach the damping scale (2.55) is recorded on a zero thickness last scattering surface. The solid line represents the method adopted for our computation. It takes into account the finite thickness for the last scattering surface. In this computation we used $\Omega_m h^2 = 0.25$ and $\Omega_b h^2 = 0.03$.

Well before recombination high electron density ensures that the ionization maintains chemical equilibrium. In these conditions the *Saha equation* holds:

$$\frac{1-x}{x^2} = \frac{4\sqrt{2}\zeta(3)}{\sqrt{\pi}}\eta \left(\frac{T}{m_e}\right)^{3/2} e^{B_1/T} \qquad (2.60)$$

where η is the baryon-photon ratio, n_b/n_γ, and $B_1 = m_e e^4/2 = 13.6$ eV is the ground state binding energy in which e is the unit charge.

We apply the analytic Saha equation in temperatures greater than 5000 K. This corresponds to ionization fractions greater than 0.999.

Peebles[23] investigated recombination in settings similar to ours (i.e. no helium) in 1968. To describe the time evolution of the ionization fraction he came up with the following differential equation:

$$\frac{\mathrm{d}x}{\mathrm{d}\eta} = aC_r \left[\beta(T_b)(1-x) - n_H \alpha^{(2)}(T_b)x^2\right] \qquad (2.61)$$

Here $\beta(T_b)$ is the collisional ionization rate from the ground state, $\alpha^{(2)}(T_b)$ is the recombination rate to excited states and C_r is a reduction factor, the fraction of net

decay rate and sum of decay and ionization rates. They are defined as

$$\beta(T_b) = \left(\frac{m_e T_b}{2\pi}\right)^{3/2} e^{-B_1/T_b} \alpha^{(2)}(T_b) \tag{2.62}$$

$$\alpha^{(2)}(T_b) = \frac{64\pi}{(27\pi)^{1/2}} \frac{e^4}{m_e^2} \left(\frac{T_b}{B_1}\right)^{1/2} \phi_2(T_b) \tag{2.63}$$

$$\phi_2(T_b) \approx 0.448 \log\left(\frac{B_1}{T_b}\right) \tag{2.64}$$

$$C_r = \frac{\Lambda_\alpha + \Lambda_{2s\to 1s}}{\Lambda_\alpha + \Lambda_{2s\to 1s} + \beta^{(2)}(T_b)} \tag{2.65}$$

$$\beta^{(2)}(T_b) = \beta(T_b) e^{+2\pi v_\alpha/T_b} \tag{2.66}$$

$$\Lambda_\alpha = \frac{8\pi \dot{a}}{a^2 \lambda_\alpha^3 n_{1s}} \tag{2.67}$$

$$\lambda_\alpha = \frac{1}{v_\alpha} = \frac{8\pi}{3B_1} = 0.617 \text{ eV}^{-1}, \tag{2.68}$$

where $\Lambda_{2s\to 1s} = 5.413 \cdot 10^{-15}$ eV is the two-photon decay rate from $2s$ state and n_{1s} is the number density of hydrogen atoms in the ground state. We categorically approximate $n_{1s} = (1-x)n_H$, placing all of the recombined hydrogen in the ground state.

The notation presented here is from Ma and Bertschinger[21], with the modification that we use natural units. Both the Saha equation and the solution to the Peebles differential equation are plotted in Figure 2.2.

Prior to decoupling the photon and baryon temperatures are the same, giving $T_b = T_\gamma \equiv T$. Ma and Bertschinger present a simple thermodynamic differential equation to integrate the baryon temperature after the decoupling. It is however coupled to the ionization fraction, making it somewhat cumbersome to evaluate. We found that extending the above temperature approximation over the period of recombination produced a relative error of no more than 10^{-6} and choose not to incorporate the temperature equation into our calculations.

Having now a model for the ionization fraction we are able to compute the electron density and using that, the derivative for optical depth. That derivative, in turn, is used to integrate the values of optical depth backwards from present day. The evolution of electron number density and optical depth are depicted in Figure 2.2.

2.3   Tightly Coupled Limit

Before recombination the rapid interaction of photons and baryons via Thomson scattering ensures that the two fluids evolve together with common velocity. Under these conditions we may expand (2.38) in terms of $1/\tau'$, where the collision rate, $\tau' = -an_e\sigma_T$, is assumed to be large.

Ma and Bertschinger[21] (1995) describe the tightly coupled limit through the velocity perturbations of the coupled photon-baryon fluid. First eliminate the collision rate, τ', in baryon velocity equation (2.38) by the photon velocity (dipole) equation (2.32), yielding:

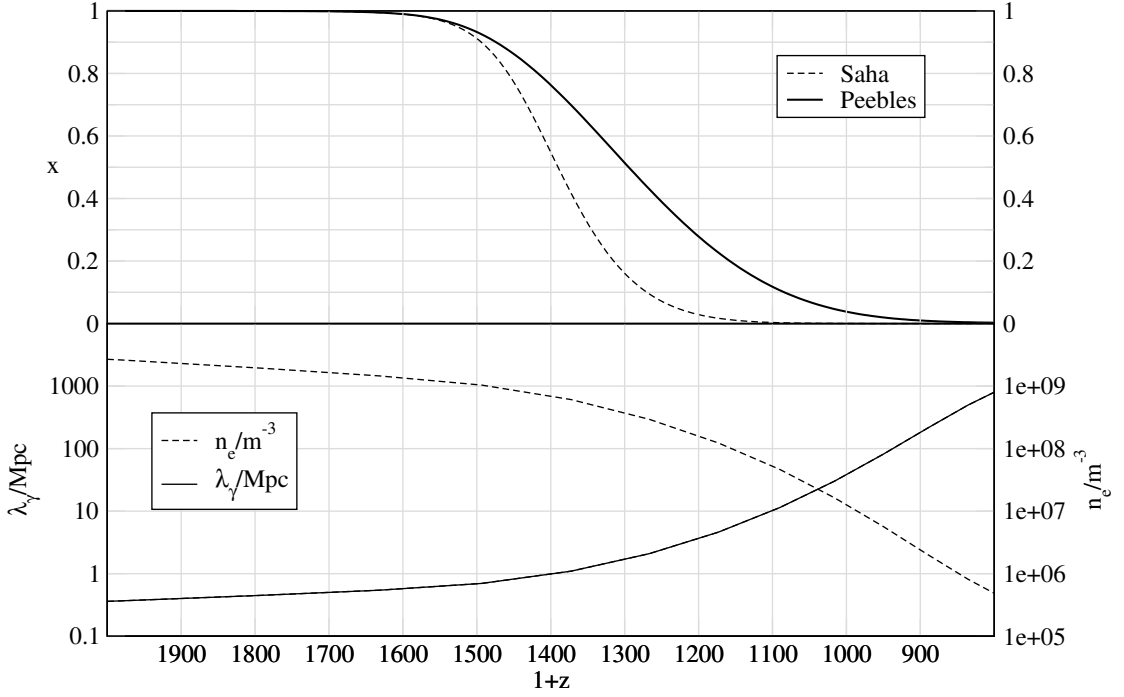$$(1+R)v_b' + R\mathcal{H}v_b - k\Theta_0 + (3\Theta_1' - v_b') = (1+R)k\Phi \tag{2.69}$$

Figure 2.2: Ionization fraction (x), photon mean free path (λ_γ) and electron density in a model, for which $\Omega_m h^2 = 0.25$ and $\Omega_b h^2 = 0.03$. The Saha equation assumes equilibrium but the actual reaction rates fail to maintain it which leads to slower decrease in the ionization fraction.

if we then solve for $(v_b - 3\Theta_1)$ in (2.38), differentiate with respect to conformal time and apply (2.69) we find

$$v_b' - 3\Theta_1' = \frac{2}{1+R}\mathcal{H}(v_b - 3\Theta_1) -$$
$$\frac{R}{\tau'(1+R)}\left[-(\mathcal{H}' + \mathcal{H}^2)v_b - \mathcal{H}k\left(2\Theta_0 + \Phi\right) - k\Theta_0'\right] + O(1/\tau'^2) \quad (2.70)$$

Equation (2.69) also solves for $3\Theta_1'$:

$$3\Theta_1' = -R\left(v_b' + \mathcal{H}v_b\right) + k\Theta_0 + (1+R)k\Phi \quad (2.71)$$

To use these we first insert (2.70) into (2.69) yielding an equation for v_b':

$$(1+R)v_b' + R\mathcal{H}v_b - k\Theta_0 - \frac{2}{1+R}\mathcal{H}(v_b - 3\Theta_1)$$
$$-\frac{R}{\tau'(1+R)}\left[-(\mathcal{H}' + \mathcal{H}^2)v_b - \mathcal{H}k\left(2\Theta_0 + \Phi\right) - k\Theta_0'\right] = (1+R)k\Phi. \quad (2.72)$$

where we have made the tight coupling approximation and dropped the $O(1/\tau'^2)$ terms.

From (2.72) we can solve for v_b' and substitute into (2.71) to compute Θ_1' in (2.71). The use of these expressions significantly reduces the amount of CPU time needed for the integration of the perturbations in the early universe. Following Ma and Bertschinger we apply the tight coupling approximation until the photon temperature drops to $2 \times 10^4 K$. The applicability of this limit was tested against the slower method and was found satisfactory.

2.4   Perturbation Equations

From Equations (2.30)-(2.38), omitting the multipoles higher than the dipole ($\ell \leq 1$), we have a set of equations:

$$\Phi' = -\mathcal{H}\Phi - \frac{1}{3\mathcal{H}} \left[k^2\Phi + 4\pi Ga^2(\rho_c\delta_c + \rho_b\delta_b + 4\rho_\gamma\Theta_0) \right] \tag{2.73}$$

$$\Theta_0' = \Phi' - k\Theta_1 \tag{2.74}$$

$$\Theta_1' = \frac{k}{3}(\Theta_0 + \Phi) - \tau'(\frac{1}{3}v_b - \Theta_1) \tag{2.75}$$

$$\delta_c' = 3\Phi' - kv_c \tag{2.76}$$

$$v_c' = k\Phi - \mathcal{H}v_c \tag{2.77}$$

$$\delta_b' = 3\Phi' - kv_b \tag{2.78}$$

$$v_b' = k\Phi - \mathcal{H}v_b - \tau'\frac{4\rho_r}{3\rho_b}(3\Theta_1 - v_b) \tag{2.79}$$

2.4.1   Initial Conditions

To actually attain numerical results we also need to initialize the perturbations at some early enough time. The criterion for this is, that the scales that are considered should be outside the horizon, retaining their inflation inherent values as we start to track their evolution. To formalize this we require[16, 5] that

$$k\eta \simeq \frac{k}{\mathcal{H}} \ll 1 \tag{2.80}$$

enabling us to drop terms proportional to k in the evolution equations. The second form is due to the fact that under radiation domination $a \propto \eta$ and

$$\mathcal{H} = \frac{a'}{a} \stackrel{\text{rad.dom.}}{=} \frac{1}{\eta} \tag{2.81}$$

The tight coupling approximation, expected to be applicable at early times, assures that $|\tau'| \gg 1$ and thus as a zeroth order approximation we drop all other terms from (2.79) and find:

$$3\Theta_1 - v_b = v_\gamma - v_b = 0. \tag{2.82}$$

Furthermore we are considering a radiation dominated epoch, so $\rho_c, \rho_b \ll \rho_\gamma$.

Given these approximations and the perturbed Einstein equations[16, 17] one can relate the initial perturbation values to the primordial curvature and entropy perturbations $\mathcal{R}$ and $\mathcal{S}$:

$$\mathcal{R} = -\Psi - \frac{2}{3(1+w)} \left(\frac{\Psi'}{\mathcal{H}} + \Phi \right) \quad \text{and} \quad \mathcal{S} = \mathcal{H} \left(\frac{\delta p}{p'} - \frac{\delta\rho}{\rho'} \right) \tag{2.83}$$

Although it is possible to consider models where both these perturbations are present, a zero entropy perturbation is consistent with the observations[18]. For simplicity we will study only adiabatic modes, setting $\mathcal{S} = 0$. The applicability of the curvature perturbation is based on the notion that for scales outside the horizon, during the radiation dominated era, it settles to a constant value.

Application of the described approximations to our perturbation Equations (2.73)-(2.79) allows to write the perturbations as functions of the constant curvature perturbation. The computation and the results are described in [16, 20]. For the initial values we will set the curvature perturbation to unity: $\mathcal{R} = 1$ (in order to find the transfer function) and from that

$$\Phi = -\frac{2}{3}\mathcal{R} = -\frac{2}{3} \tag{2.84}$$

$$\Theta_0 = -\frac{1}{2}\Phi = \frac{1}{3} \tag{2.85}$$

$$\Theta_1 = \frac{1}{6}k\eta\Phi = -\frac{1}{9}k\eta \tag{2.86}$$

$$\delta_c = \delta_b = -\frac{3}{2}\Phi = 1 \tag{2.87}$$

$$v_c = v_b = \frac{1}{2}k\eta\Phi = -\frac{1}{3}k\eta. \tag{2.88}$$

Chapter 3

Results

In order to study the evolution of the perturbations we applied an adaptive step size Runge-Kutta-Fehlberg algorithm to the set of differential equations (2.73)-(2.79). The delta function approximation performed on the visibility function made it necessary to record only the values of the perturbations at decoupling. This turned out to provide us with a useful tool in the study of the parameter effects. Because they vary smoothly as functions of k, we were able to collect them in a grid and then interpolate them using cubic splines[7]. Both the DE-solver and the spline routines are implemented in the Gnu Scientific Library[8] (GSL).

The only exception were the integrated Sachs-Wolfe effects that are handled in a different manner.

3.1   Integration of the Perturbations

As a first approximation we started our numerical calculations with a model, in which baryons and the corresponding perturbations were omitted. This is not a very realistic model, as there is no recombination without baryons. It did, however, provide as with some insight in whether or not the group of differential equations was *stiff* or not. Stiff differential equations are such, that their solutions have multiple different timescales[7], and therefore require implicit methods to be integrated efficiently.

We concluded, that although the stiffness of the system did increase somewhat as k was increased, no actual gain in speed was accomplished resorting to more complex, implicit methods. For this experiment the full range of GSL-provided ODE solvers were tried out.

Adding the baryon equations to the system changed the situation completely. The tight coupling between the photon and baryon equations introduced a whole new time scale requiring as much as over 7 minutes to integrate the equations with a single value for k on a workstation. The saving grace here is, that the coupling could be approximated as described in section 2.3.

Applying the tight coupling approximation to the coupled photon-baryon fluid before recombination reduced the time needed to complete the integration to less than half a minute. This is an over ten-fold speedup.

The time evolution of the perturbations in different Fourier modes can be viewed from Figures 3.1 and 3.2 and the effect of baryon and matter contents upon them from Figures 3.3 and 3.4. The effect of the density parameters will be the subject of sections

to follow.

For the remainder of this thesis we will scale all conformal time coordinates with $H_{100}^{-1} \approx 9.78 \cdot 10^9 a$ and Fourier modes with $H_{100} \approx (2998 \, \text{Mpc})^{-1}$.

ω_m	h	$\eta_{\text{eq}}/H_{100}^{-1}$	$\eta_{\text{dec}}/H_{100}^{-1}$
0.10	0.316	0.053	0.105
0.20	0.447	0.027	0.088
0.30	0.548	0.018	0.077

Table 3.1: Matter-radiation equality and decoupling in different ω_m models

For the purpose of computing the angular power spectrum (Section 2.2), we record the perturbation values only at decoupling. It is crucial to notice, that small angular scales (large k), are damped exponentially with respect to the Fourier wave number k, before the photons and baryons decouple. Therefore integration of the decoupling values over k-axis receives its significant contributions from the beginning of the axis. This being the case it is not feasible to use a coordinate transformation in order to map the infinite k-axis to a finite interval. In practice we only need to integrate the differential equations for $k/H_{100} < 10^4$.
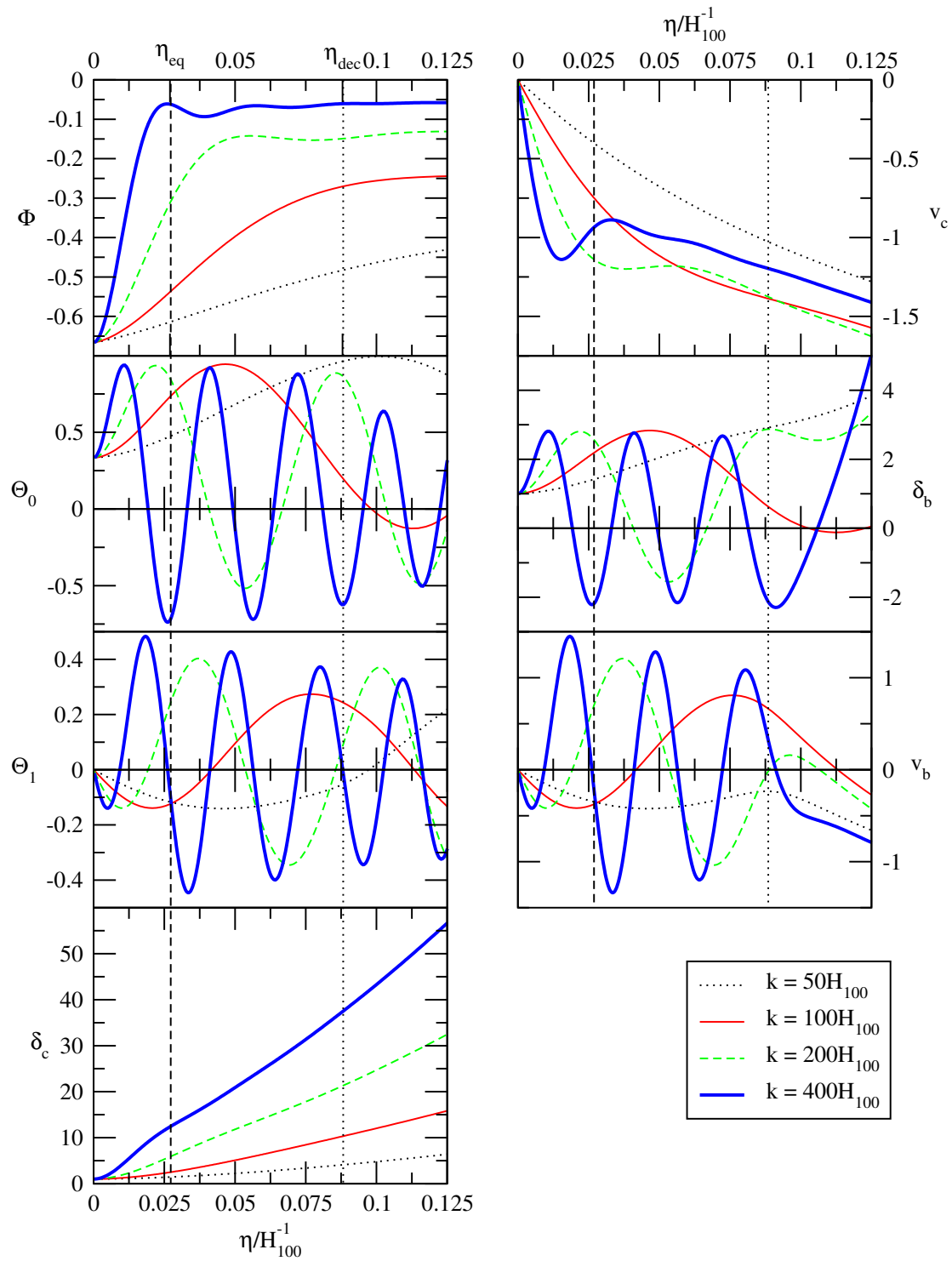
Figure 3.1: The time evolution of the perturbations for multiple Fourier modes presented first without the added diffusion damping. These are the numerical solutions for the differential equations (2.73)-(2.79) with the initial values (2.84)-(2.88). In this model $\Omega_m h^2 = 0.20$ and $\Omega_b h^2 = 0.03$. The matter-radiation equality occurs at $\eta/H_{100}^{-1} = 0.027$ (the slashed vertical lines) and the decoupling takes place roughly at $\eta/H_{100}^{-1} = 0.088$ (the dotted vertical lines). η_0 is approximately at $\eta/H_{100}^{-1} = 4.32$.
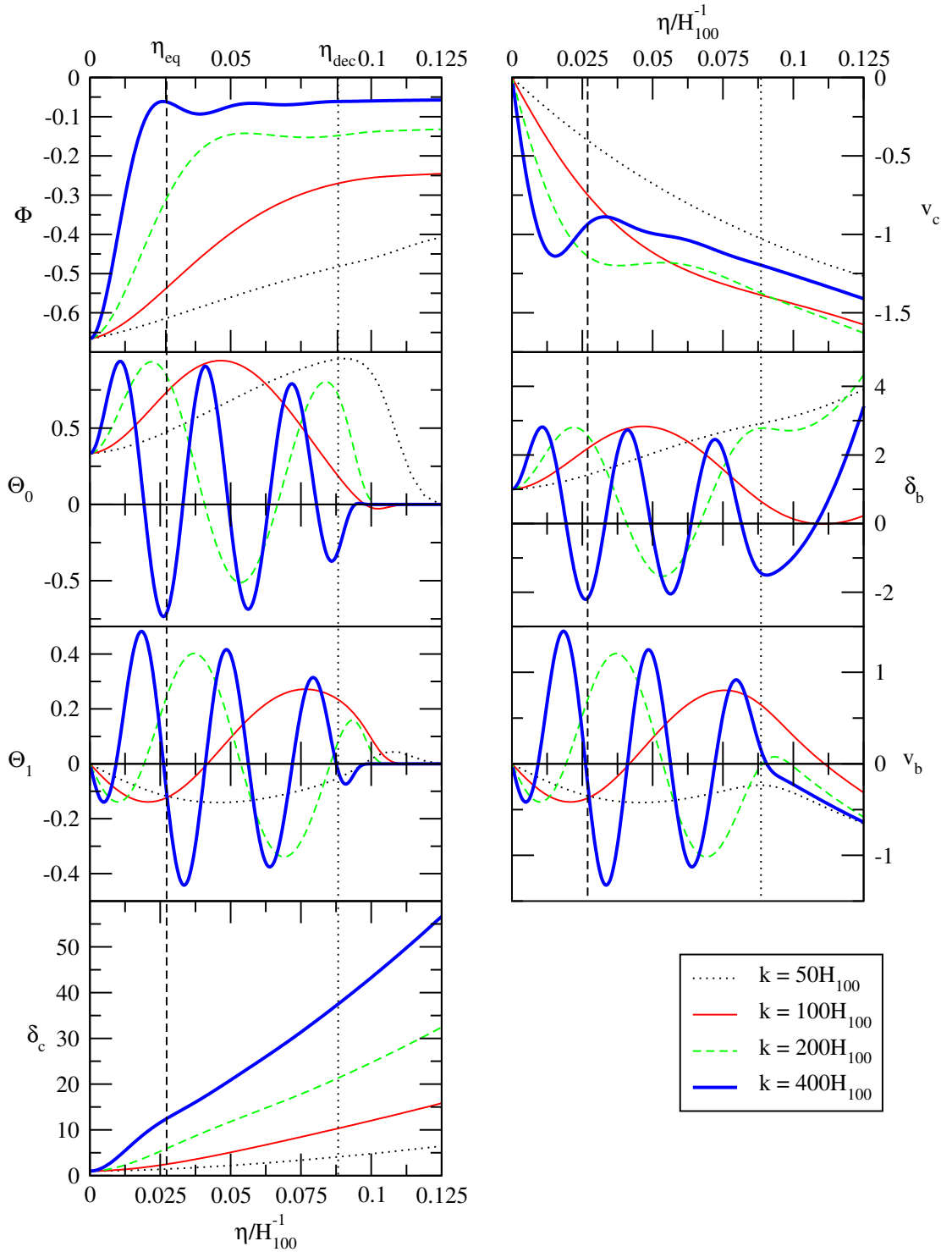
Figure 3.2: The time evolution of the perturbations for multiple Fourier modes with diffusion damping. In this model $\Omega_m h^2 = 0.20$ and $\Omega_b h^2 = 0.03$. The matter-radiation equality occurs at $\eta/H_{100}^{-1} = 0.027$ (the slashed vertical lines) and the decoupling takes place roughly at $\eta/H_{100}^{-1} = 0.088$ (the dotted vertical lines). η_0 is approximately at $\eta/H_{100}^{-1} = 4.32$.
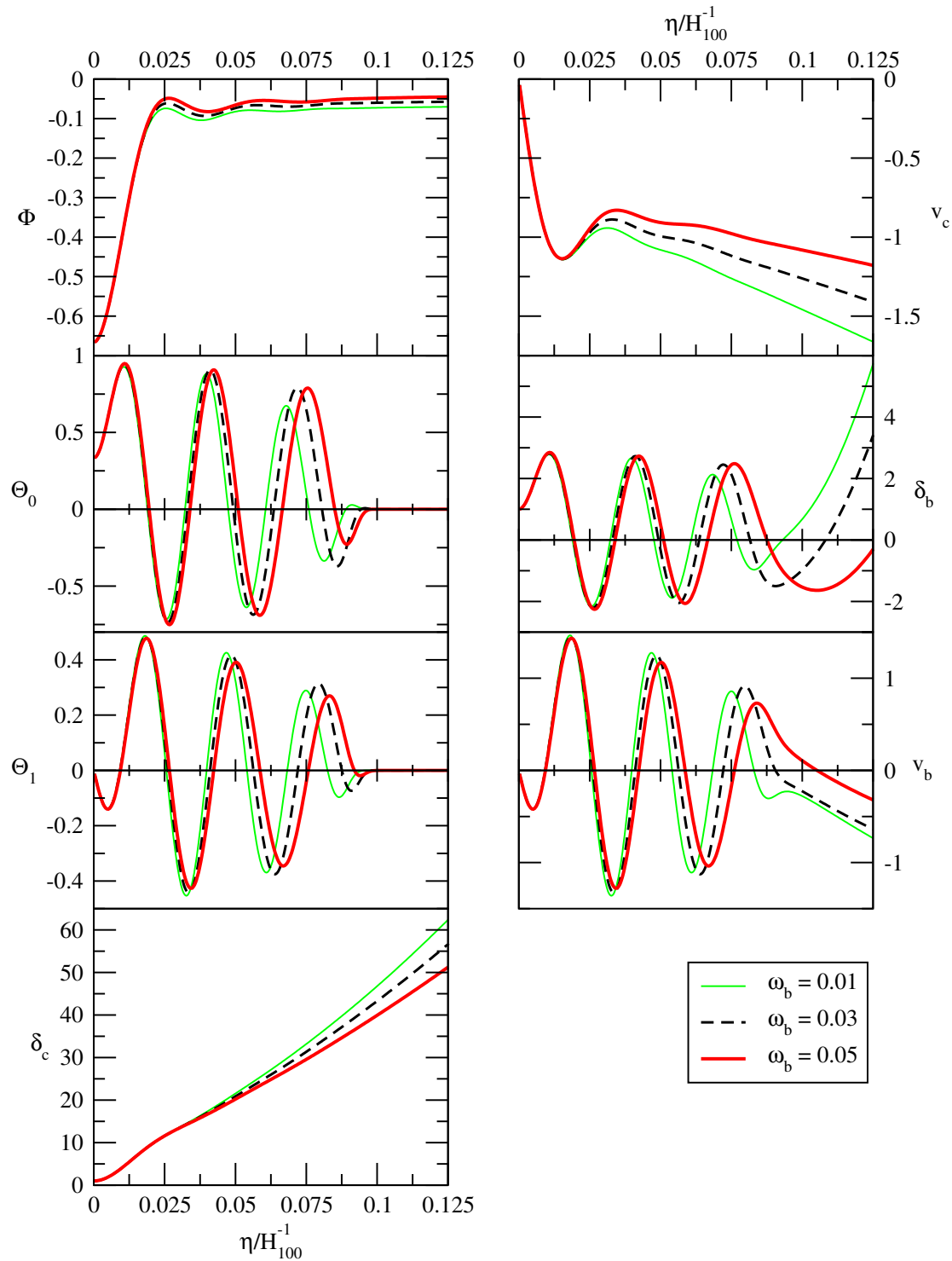
Figure 3.3:   The time evolution of the perturbations with different baryon energy densities. Here $\omega_m = 0.20$ and $k = 400H_{100}$. Decoupling takes place roughly at $\eta/H_{100}^{-1} = 0.087$. Increasing the baryon density actually delays the decoupling time as the peak of the visibility function is shifted forward in time (cf. Figure 3.5). Also the addition off baryons decreases the sound speed, which in turn lengthens the period of the oscillations.
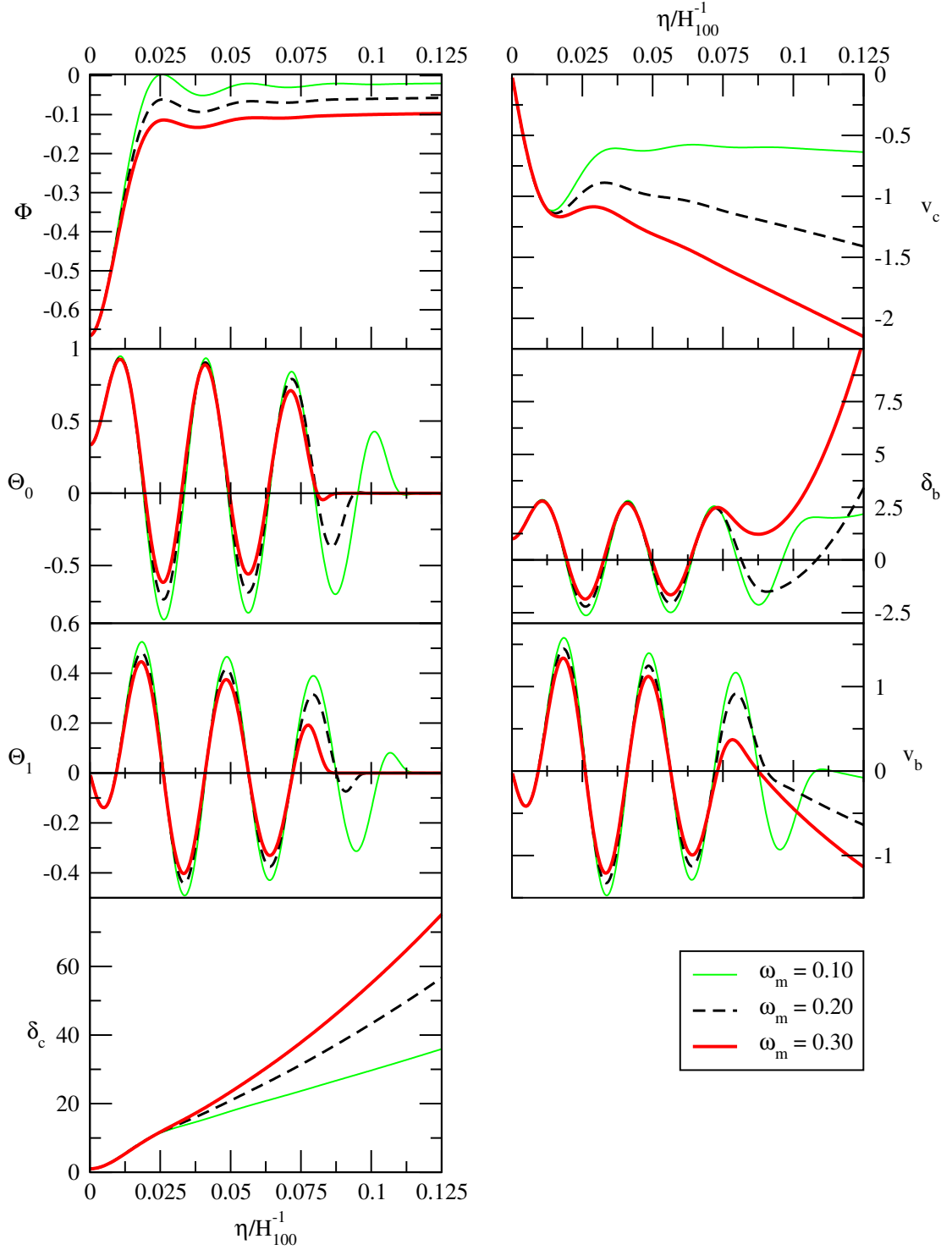
Figure 3.4: The time evolution of the perturbations with different matter energy densities. Here $\Omega_b h^2 = 0.03$ and $k = 400 H_{100}$. Matter-radiation equality and the time of decoupling vary as a function of ω_m and are both advanced by increment of the matter density (see Table 3.1).

Figures 3.5 and 3.6 represent the damping scale and the visibility function for different baryon and matter densities. They show that both matter and baryon densities shift the decoupling, but in their own, characteristic way. Since decoupling is brought on by the weakening interactions of photon and baryon fluids, it can be considered to occur once the collision rate ($\sim a n_e$) drops below some limit. Baryon density is related to the overall electron density. Adding baryons will provide more electrons and thus the ionization fraction will need to drop more to yield the same free electron density and allow decoupling. Therefore increasing baryon density will delay decoupling.

For matter density the process is more complicated. Adding matter will shift the matter-radiation equality. Since matter has negligible pressure, the rate of expansion changes. A universe with more matter will also expand faster, leading to earlier decoupling. This effect is rather virtual, since the scale factor and redshift of decoupling are not affected. The subject is developed further in section 3.2.

Be sure to note two important features of the evolution of these perturbations. First, if you look at the upper left corner in Figures 3.1-3.4, you see the gravitational potential, Φ, decay upon the horizon entry of the scale. For small scales (large k) that enter during radiation domination the effect is far more stronger than for larger scales that enter after matter-radiation equality, η_{eq}. Gravitational potential perturbation reflects the inhomogeneity of energy density in the universe. During expansion static energy density would just decrease, but the gravitation of these inhomogeneities attract more matter and radiation. This process opposes the expansion-related decay of Φ. For radiation, the concentration of energy is impeded by radiation pressure. As a result, gravitational potentials decay heavily during the radiation dominated epoch. This applies for scales that evolve, i.e. are in causal contact (within the horizon), prior to matter-radiation equality.

Next compare the differential equations of CDM and baryons:

$$\delta_c' = 3\Phi' - kv_c \tag{3.1}$$

$$v_c' = k\Phi - \mathcal{H}v_c \tag{3.2}$$

$$\delta_b' = 3\Phi' - kv_b \tag{3.3}$$

$$v_b' = k\Phi - \mathcal{H}v_b - \tau'\frac{4\rho_r}{3\rho_b}(3\Theta_1 - v_b). \tag{3.4}$$

Aside from the collision term due to photon-baryon coupling the equations are the same. Looking now at Figure 3.3 you can see this making a huge difference in the behavior of the perturbations as the baryon variables oscillate with the photon multipoles. Tight coupling does indeed assure, that photons and baryons behave as a single fluid.
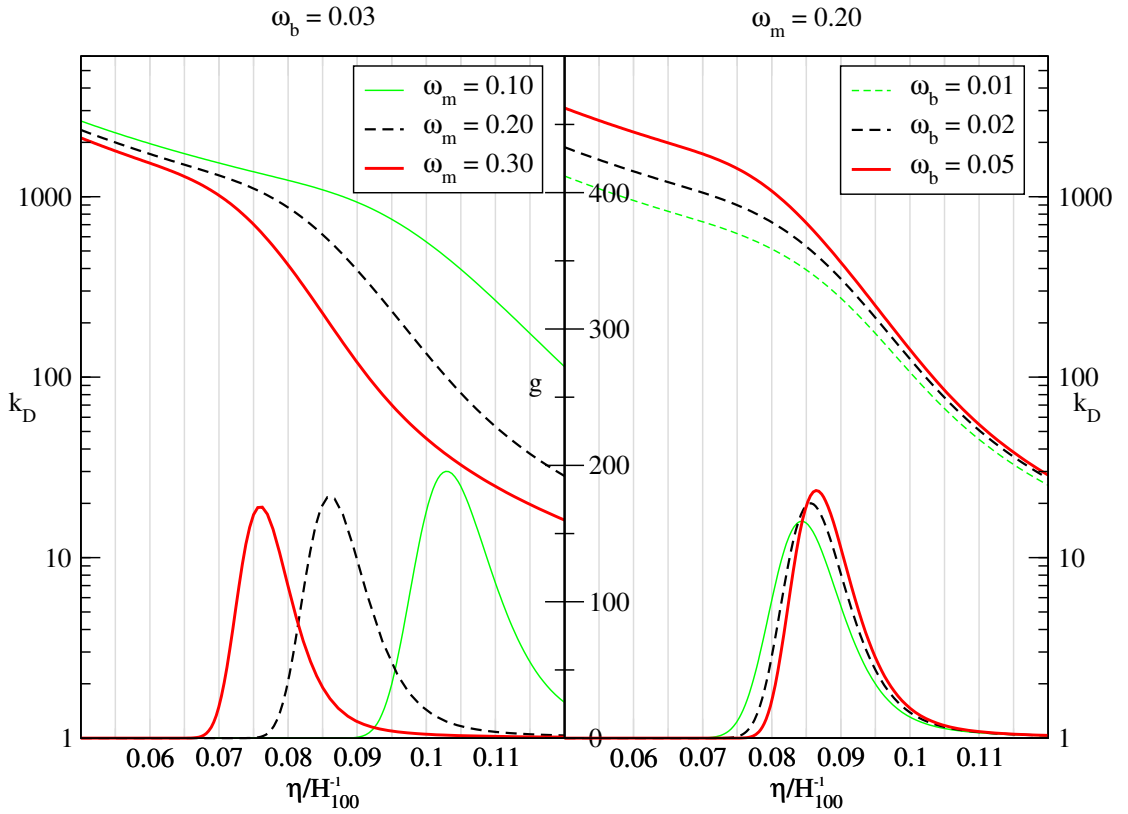
Figure 3.5: Both the visibility function, $g(\eta)$ and the damping scale, k_D are affected by the matter and baryon densities of the universe. In the figures the peaked shapes are the visibility functions that are approximated by a delta function in line-of-sight integration. They corresponds to the linear scale in the center. You should note from the figure, how increase in the matter density advances and in the baryon density delays decoupling (shifts the peak of the visibility function). In these plots the normalization of $g(\eta)$ is a function of H, not unity.
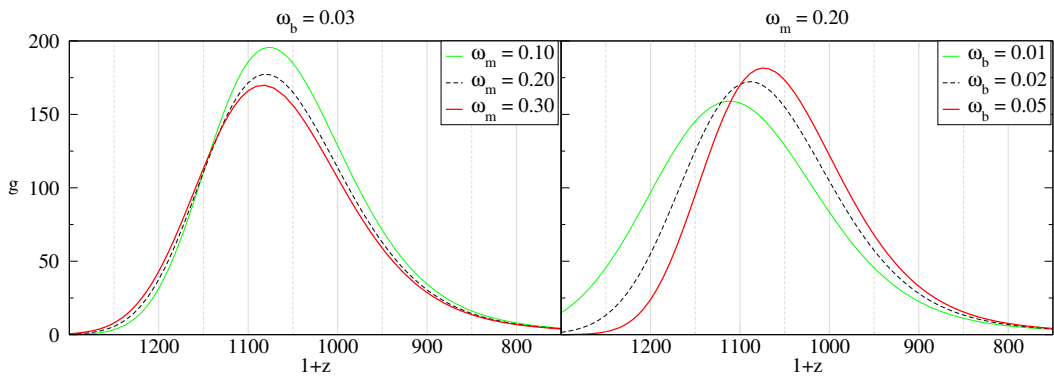

Figure 3.6: Plotted against conformal time the peak of the visibility function appears to advance with increasing matter density (cf. Fig. 3.5). However matter also changes the expansion of the universe. This plot with the visibility function against cosmic redshift shows, that the redshift of CMB photons depends very little on the matter density. The plot on the right shows, that the delay of decoupling due to baryon density is real. In a high baryon density model the cosmic redshift to the last scattering is lower.

3.2   Components of the Angular Power Spectrum

Let us review the final result in our line-of-sight integration:

$$\Theta_\ell(\eta_0, k) = [\Theta_0(\eta_{\text{dec}}, k) + \Phi(\eta_{\text{dec}}, k)]j_\ell[k(\eta_0 - \eta_{\text{dec}})]$$
$$+3\Theta_1(\eta_{\text{dec}}, k)j'_\ell[k(\eta_0 - \eta_{\text{dec}})]$$
$$+2\int_0^{\eta_0} e^{-\tau}\Phi'(\eta, k)j_\ell[k(\eta_0 - \eta)]\text{d}\eta. \tag{3.5}$$

It has five ingredients, that all vary in respect to k. They divide into three categories

- Perturbation values at decoupling: $\Theta_0(\eta_{\text{dec}}, k), \Theta_1(\eta_{\text{dec}}, k)$ and $\Phi(\eta_{\text{dec}}, k)$.

- Spherical Bessel functions and their derivatives: $j_\ell[k(\eta_0 - \eta_{\text{dec}})]$ and $j'_\ell[k(\eta_0 - \eta_{\text{dec}})]$.

- Integrated Sachs-Wolfe term

In the following we will discuss these categories separately.

3.2.1   Perturbation Values at Decoupling

The two remaining photon multipole moments that we keep in our approximation are Θ_0 and Θ_1. Instead of the monopole Θ_0, which is proportional to the photon energy density perturbation, we will encounter and utilize the effective temperature perturbation $(\Theta_0 + \Phi)$. As discussed in conjunction with the Sachs-Wolfe effect, adding the gravitational perturbation actually negates the potential differences between the source and the observer. Thus the perturbations of the effective temperature correspond to actual temperature fluctuations of the CMB.

The decoupling values as functions of the Fourier mode are oscillating functions with a decreasing amplitude: the effects of diffusion damping strengthen as the Fourier wave number increases. These two properties dominate also their decoupling values with respect to k. According to Figure 3.7 these values oscillate as a function of k, with a period not much smaller[1] ($\sim 300H_0$) than the scale at which these oscillations are damped ($\sim 1200H_0$). That is, as we integrate over a few damping scales we only require a handful of data points in that interval for decoupling values to accurately interpolate them between the data points. This supports the notion made earlier about the applicability of spline interpolation to the decoupling values.

The integral for C_ℓ is evaluated for every required ℓ separately, but the perturbation values remain unchanged, so the spline interpolants need to be constructed only once. Since the angular power spectrum is also smoothly oscillating as a function of ℓ, it also can be approximated using splines[12]. Later on their evaluation and even integration can be done with a fraction of the time cost of actually integrating the differential equations.

3.2.2   Spherical Bessel Functions and Their Derivatives

The impact of evaluating spherical Bessel functions j_ℓ on the scalability of our computation is considerable. The GSL library provides multiple different algorithms to evaluate

---

[1]The oscillation period is determined by the sound horizon. Details will be presented with baryon oscillations in Section 3.3.
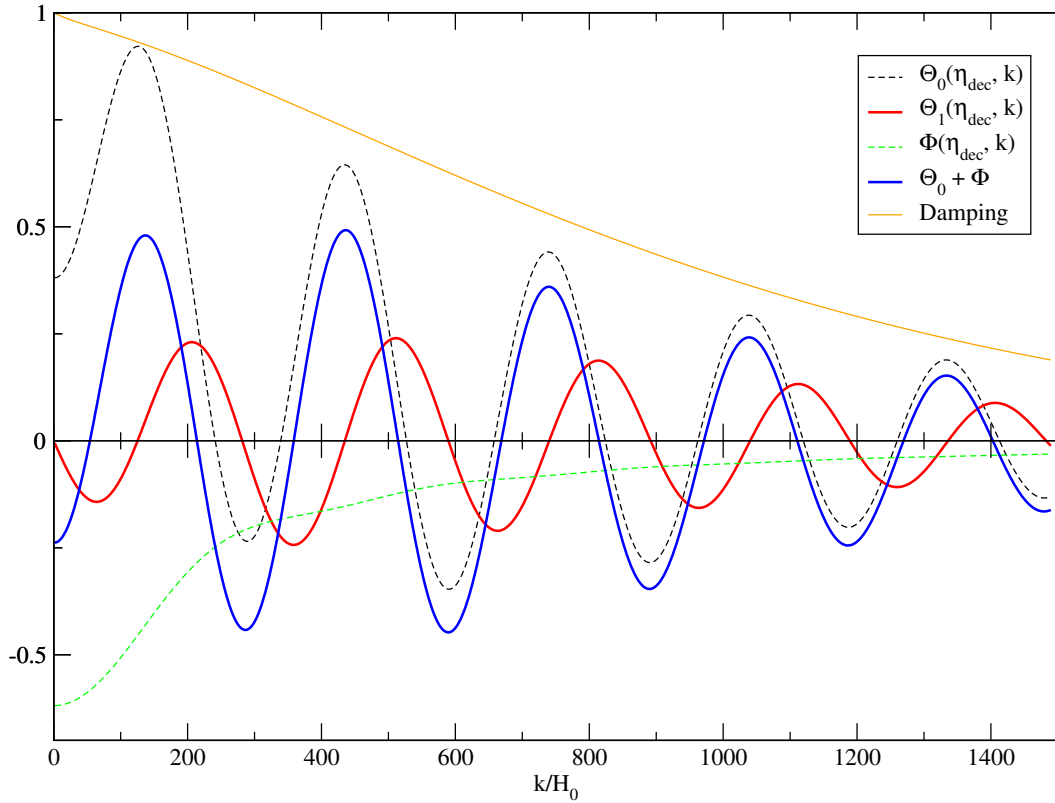
Figure 3.7: Decoupling values of the perturbations for $\Omega_m h^2 = 0.20$ and $\Omega_b h^2 = 0.03$.

spherical Bessel functions. Because most of these algorithms use recursion relations to reach desired j_ℓ and are able to return also the intermediate stages, it makes sense to compute these values in advance. Since these functions are not dependent on the model, we wrote a program that creates a table of the spherical Bessel functions for $\ell = 2..2000$ in a range $0..10000$ and stride 1.5. After the table is created once, it can be loaded during program execution and used to initialize splines.

The generation of the spherical Bessels requires great care, because the recursion relations easily lead to over- and underflows due to limited precision. Only after trial and error we were able to determine the ranges in which the supplied generation algorithms produced satisfactory results.

Some of the spherical Bessel functions are plotted in Figure 3.8

For the integral of spherical Bessel functions, an analytical result exists,

$$\int_0^\infty \mathrm{d}x \, x^{n-2} j_\ell^2(x) = 2^{n-4} \pi \frac{\Gamma(\ell + \frac{n}{2} - \frac{1}{2})\Gamma(3-n)}{\Gamma(\ell + \frac{5}{2} - \frac{n}{2})\Gamma^2(2 - \frac{n}{2})} \tag{3.6}$$

for $n = 1$ this reads

$$\int_0^\infty \frac{\mathrm{d}x}{x} j_\ell^2(x) = \frac{1}{2\ell(\ell+1)} \tag{3.7}$$
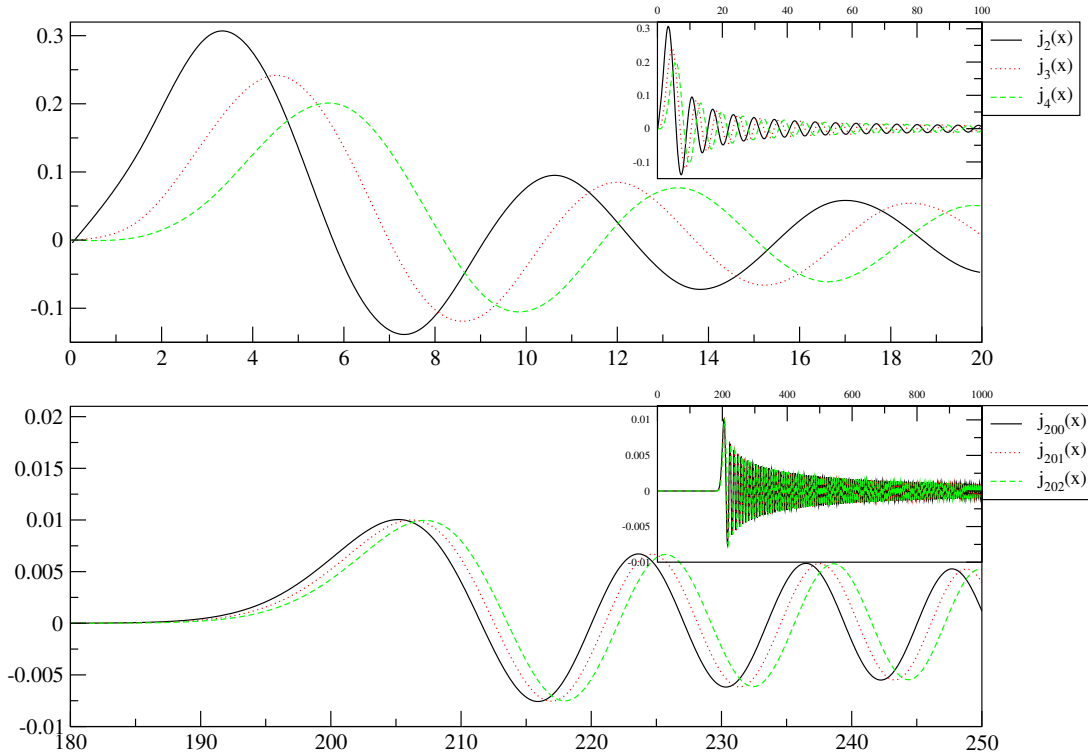
Figure 3.8: Spherical Bessel functions have their first peak near $x = \ell$. As ℓ increases, the oscillation frequency and the relative difference between the first and the following peaks decrease. This means, that to integrate over, say 99% of the area of j_ℓ^2 one needs to cover an increasing strip of the x-axis. The very weak beginning before the first peak is prone to produce numerical errors because of underflow. Our program approximated it to zero up to a point where double precision was sure to suffice.

and from the above we can also derive

$$\int_0^\infty \frac{\mathrm{d}x}{x} j_\ell'^2(x) = \frac{1}{6\ell(\ell - 1)}. \tag{3.8}$$

The latter formula is derived using the derivative of a spherical Bessel function:

$$j_\ell'(x) = j_{\ell-1}(x) - \frac{\ell + 1}{x} j_\ell(x) \tag{3.9}$$

We used equations (3.7) and (3.8) to determine the range in which the Bessel functions need to be integrated to obtain at least a precision of 1% by integrating the two expressions over definite intervals and comparing the results to the analytical expressions. This provided us with an upper limit for the C_ℓ integration interval.

3.2.3   Integrated Sachs-Wolfe Term

The redshift effects a primeval photon experiences on its journey to the observer are called Sachs-Wolfe effects on account of their paper in 1967[26].

These effects divide into two: the overall potential difference between the source and the observer and the evolution of the gravitational potential during the photon's

travel. The former is known as the *ordinary* and the latter as the *integrated* Sachs-Wolfe effects (SW and ISW). The normalization for the angular power spectrum, $\ell(\ell+1)C_\ell/2\pi$ is chosen so, that the SW effect for scales large enough to enter the horizon during matter domination is flat[16]. During matter domination, the gravitational potential Φ is constant, so we get no ISW contribution from the matter dominated era.

Although the ISW term has an inferior effect to the spectrum compared to the $\Theta_0+\Phi$ term, it is responsible for some important characteristics of the spectrum at relatively large angular scales (small ℓ). Our model does not include the dark energy that is responsible for the evolution of gravitational perturbations near the present, so we also lack the late ISW effect that manifests itself in the very first multipoles.

We do, how ever, have an early ISW effect that affects Fourier scales for which Φ has not decayed completely before recombination. For these scales Φ also has a non-negligible derivative shortly after recombination.

Let us define
$$I_{SW}(k,\ell) \equiv 2 \int_0^{\eta_0} e^{-\tau}\Phi'(\eta,k)j_\ell[k(\eta_0 - \eta)]\mathrm{d}\eta, \tag{3.10}$$
the last term of Eq. (3.5).

The $e^{-\tau}$ factor ensures that no contribution is gained from time prior to recombination. After that it is close to unity. Had the epoch during which Φ' is significant turned out to be far less than the time scale for $j_\ell[k(\eta_0 - \eta)]$, we could have approximated $j_\ell[k(\eta_0 - \eta)] \approx j_\ell[k(\eta_0 - \eta_{\mathrm{dec}})]$ and moved it out from the integral. For $j_\ell(x)$ the period was of the order ~ 10. So, denoting the length of the $\Phi'(k)$-significant period as $\triangle_k$ we can formulate this applicability condition as

$$k\triangle_k \ll 10. \tag{3.11}$$

Comparing this limit to Figure 3.9 shows, that the approximation holds for small k but breaks down around $k = 100H_0$. We will compute the I_{SW} integral with the spherical Bessel function included. However the plots also show, that for all scales considered a very good accuracy is reached integrating only up to $\eta = 0.2H_0^{-1}$ and not all the way to present day $\eta_0 \approx 2H_0^{-1}$. Hu and Sugiyama[12] estimate an error of $10-15\%$ when using the value Φ'_{dec} for the I_{SW} instead of following the evolution of $\Phi'(\eta)$. Such an approach would though require some estimate of the duration of matter-radiation co-dominance.

$I_{SW}(k,\ell)$ is plotted for a few different ℓ in Figure 3.10.

The spectrum along with all the source function components for our reference parameter values ($\omega_m = 0.20$, $\omega_b = 0.03$) can be viewed in Figure 3.11.
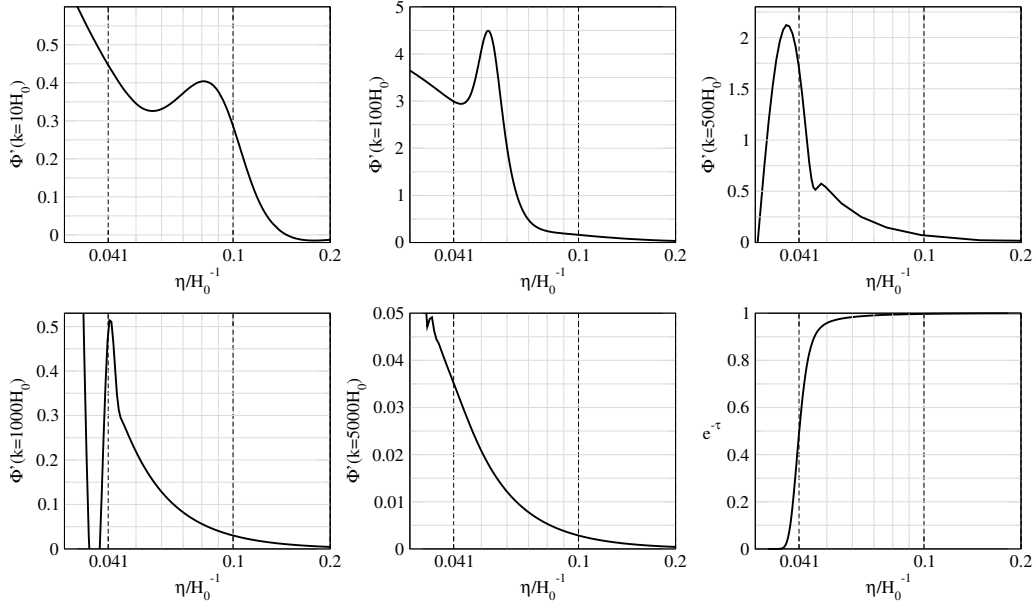
Figure 3.9: Derivatives of $\Phi(\eta, k)$ for different Fourier modes k in a model for which $\Omega_m h^2 = 0.25$ and $\Omega_b h^2 = 0.03$. Note the different scales. The decoupling is at $\eta_{\text{dec}} = 0.041 H_0^{-1}$. The rightmost plot in the lower row is $e^{-\tau}$. The up-pointing wedge which you can see in the $k = 10H_0$ and $k = 100H_0$ results from the damping of the photon monopole. For higher k the damping occurs more abruptly and this shows as by narrowing of the wedge. For high enough k the wedge peak occurs too early to contribute to the I_{SW} integral, significantly reducing the ISW term.
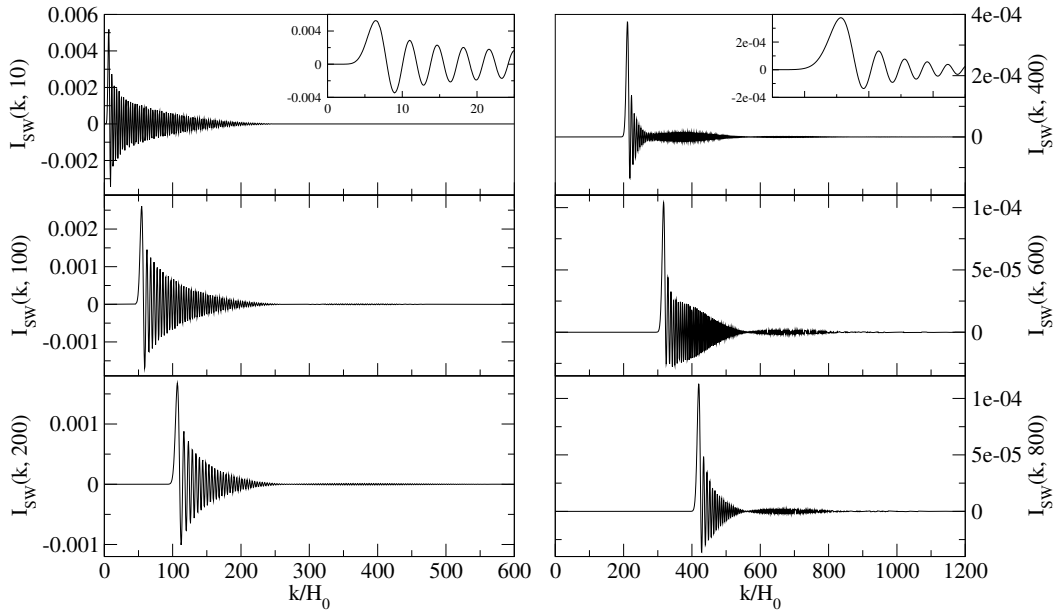

Figure 3.10: $I_{SW}(k, \ell) = 2 \int_0^{\eta_0} d\eta\, e^{-\tau} \Phi'(\eta, k) j_\ell[k(\eta_0 - \eta)]$ for $\ell = 10 - 800$. Note the different vertical scales. As can be seen from Figure 3.11, the I_{SW} contribution is most significant around $\ell = 200$ and utterly negligible for $\ell > 500$. The rapid oscillations that cause the plots appear solid are due to the spherical Bessel functions and the low frequency oscillations are from the gravitational perturbation.

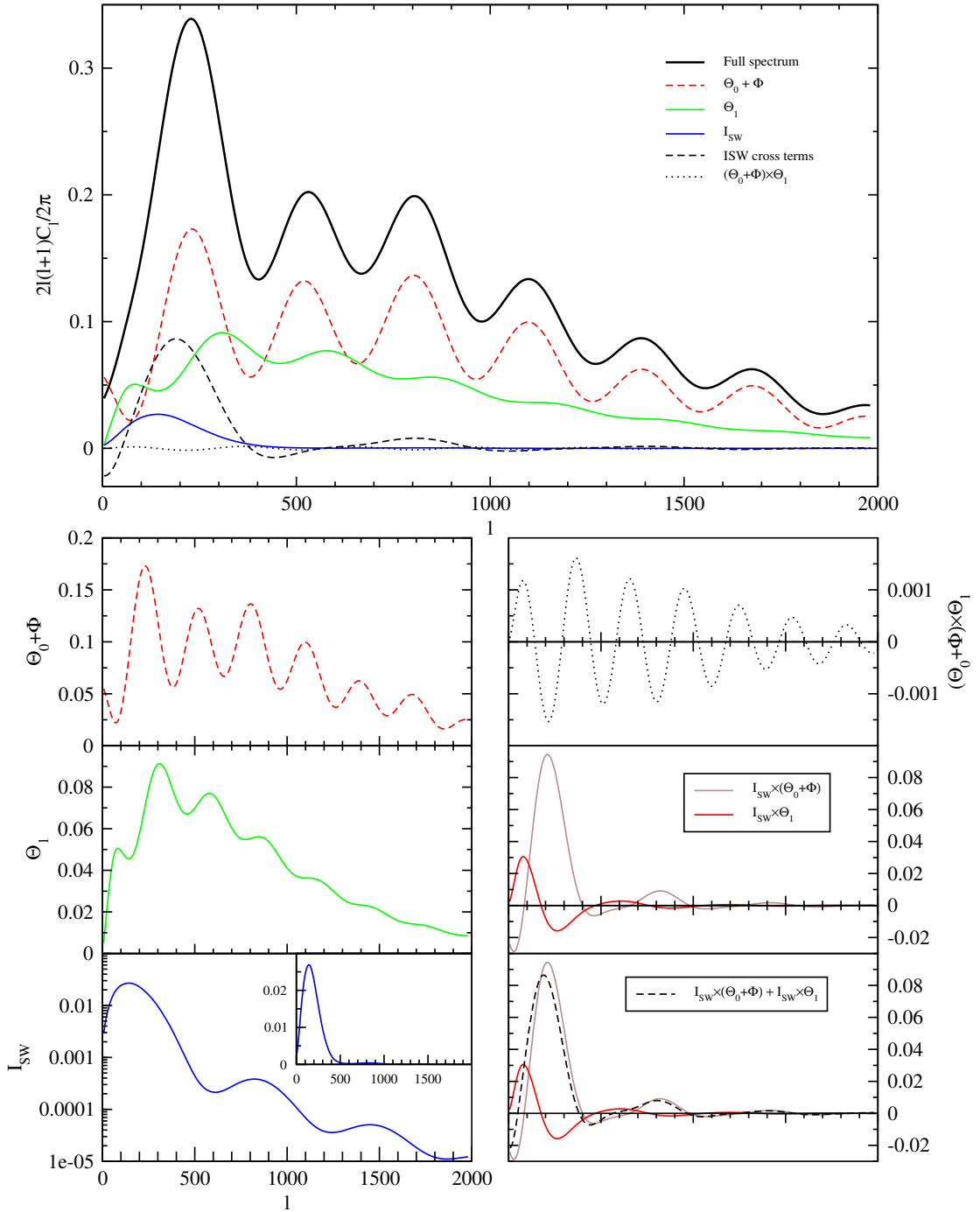Figure 3.11: The angular power spectrum $2\ell(\ell+1)C_\ell/2\pi$ and all of its components in our simplified calculation. Please take notice how the scale on the vertical axis changes between graphs. The spectrum was evaluated for an ℓ-grid with an interval of 30 and the remaining points were interpolated using cubic splines. Here we have used $\Omega_b h^2 = 0.03$ and $\Omega_m h^2 = 0.20$.

3.3   Baryon Density and the Power Spectrum

Before we may study and discuss the impact matter density has on the angular power spectrum we need to know more about the dynamics of the photon-baryon fluid. We studied the effect of baryon energy density to the power spectrum using $\omega_b \equiv \Omega_b h^2$ between 0.01 and 0.05. Setting $\omega_m = 0.20$ (our reference value) yields $h = \sqrt{\omega_m/\Omega_m} = 0.447$ and $\Omega_b = 0.0045 \ldots 0.0224$.

The oscillating pattern of the angular power spectrum is known as the acoustic, or Doppler, peaks. The former reflects better the mechanism that produces these shapes and is therefore adopted for our use. When the initial perturbations at some scale enter horizon they begin to evolve. Overdensities begin to grow, leading to temperature rise. Since the dominating energy component is initially radiation that has also pressure, the process of compression is eventually reversed. In time the pressure gradient is reversed and, with the aid of gravitation, compression begins again. This process can be considered as sound waves propagating in the photon-baryon plasma.

It is a well known fact of the trade, that as baryon density increases the odd acoustic peaks in the power spectrum strengthen and the even peaks weaken. The mechanism that transmits this effect from the acoustic oscillations of the photon-baryon fluid will be the subject of this section. Having set up this machinery from scratch we are in the position to track its propagation thoroughly.

Figure 3.12 shows this behavior of the acoustic peaks with respect to baryon energy density. There is something more to be seen here: increasing the baryon density reduces the frequency of the acoustic oscillations so the peaks occur on smaller scales (larger ℓ) than with lower baryon density. Also the damping effect that reduces the power at small scales is weaker for higher baryon densities. This is explained by looking at the damping scale calculation in Eq. (2.55): $k_D \propto \sqrt{\omega_b}$. For more graphical evidence see Figure 3.5. For comparison we created the power spectra for different baryon densities also without the damping effects. Figure 3.13 shows that without diffusion damping there is actually *more* power at small scales in low baryon density models. To discover the source of these effects we plotted the angular power spectra for the monopole $(\Theta_0 + \Phi)$ and dipole (Θ_1) terms. They are included as Figure 3.14. Since ISW affects only the first acoustic peak we could rule it out as a source of the baryon effects (it is plotted in Fig. 3.25). Clearly we need to study how the effective temperature $(\Theta_0 + \Phi)$ is related to the baryon density.

Hu and Dodelson[11] discuss the baryon effect through an oscillator equation first given in [12]. For derivation, see Appendix A:

$$c_s^2 \frac{\mathrm{d}}{\mathrm{d}\eta} \left(c_s^{-2} \Theta_0' \right) + c_s^2 k^2 \Theta_0 = -\frac{k^2}{3} \Phi + c_s^2 \frac{\mathrm{d}}{\mathrm{d}\eta} \left(c_s^{-2} \Phi' \right), \tag{3.12}$$

where the sound speed, $c_s \equiv \sqrt{\frac{p'}{\rho'}}$, now includes the baryon effect:

$$c_s^2 = \frac{\rho_\gamma'}{\rho_\gamma' + \rho_b'} c_\gamma^2 + \frac{\rho_b'}{\rho_\gamma' + \rho_b'} c_b^2 \approx \frac{1}{1 + \rho_b'/\rho_\gamma'} c_\gamma^2 = \frac{1}{3(1+R)}. \tag{3.13}$$

In the first stage we have approximated $c_b^2 \ll c_\gamma^2$. The second equality requires the use of the background continuity equation:

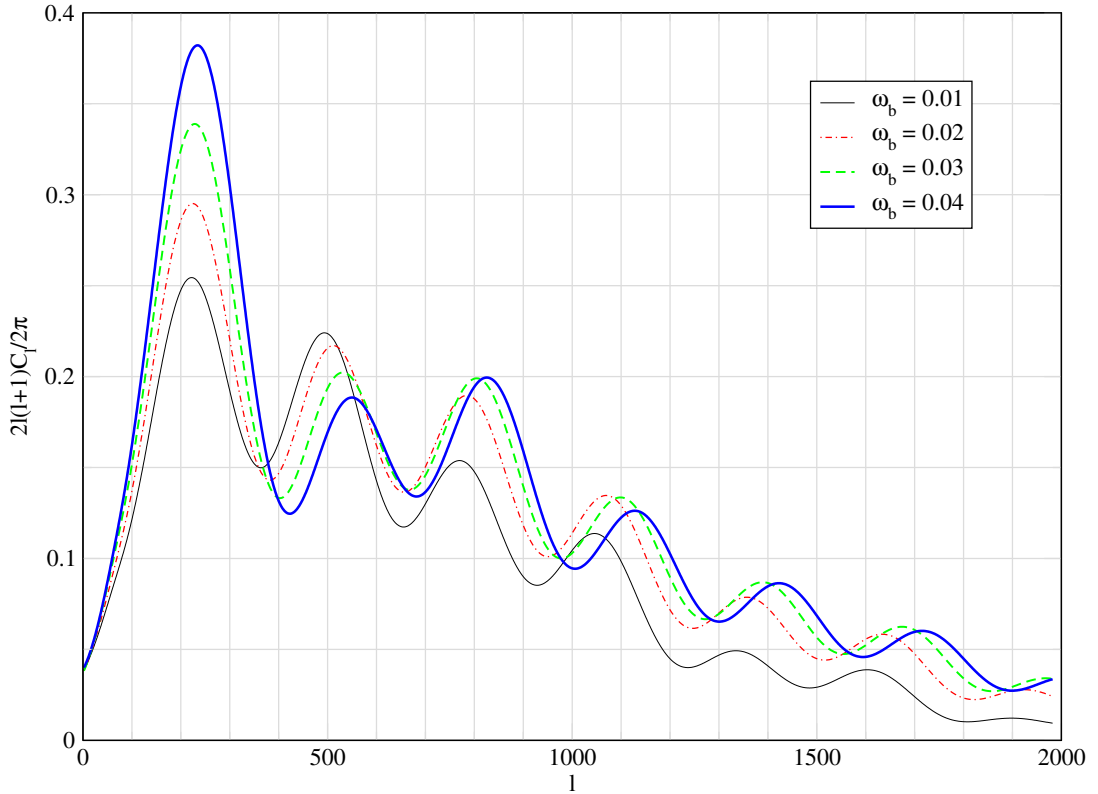$$\bar{\rho}' = -3(\bar{\rho} + \bar{p})\frac{a'}{a} \tag{3.14}$$

Figure 3.12: The angular power spectrum $2\ell(\ell+1)C_\ell/2\pi$ for different baryon energy densities. As expected, increase in Ω_b raises the first and third (odd) peaks and lowers the second and fourth (even) peaks. After these, the effect is blurred by diffusion damping that suppresses the smallest scales (large ℓ). For higher baryon densities the damping scale is smaller so the end of the spectrum is not damped as heavily. Because of damping, the overall power of the spectrum if clearly higher for high baryon density. Here we have used $\Omega_m h^2 = 0.20$.

and the fact that for radiation $c_\gamma^2 = 1/3$. c_s is the weighted average of the sound speeds of the two fluids. R is the photon-baryon momentum density ratio:

$$R = \frac{p_b + \rho_b}{p_\gamma + \rho_\gamma} \approx \frac{3\rho_b}{4\rho_\gamma}. \tag{3.15}$$

The second form is due to the fact that we approximate out baryon pressure and for radiation $p = \frac{1}{3}\rho$.

Equation (3.12) can be arranged further by applying Eq. (3.13):

$$\frac{d}{d\eta}\left[c_s^{-2}(\Theta_0' - \Phi')\right] = -k^2\left[\Theta_0 + (1+R)\Phi\right]. \tag{3.16}$$

Matter domination ends the decay of the gravitational potentials as discussed in Section 3.1. At decoupling this holds effectively only for small scales that decay earlier, but for our purposes it suffices to approximate $\Phi' = 0$. Another issue is the derivative of sound speed, or actually

$$\frac{d}{d\eta}c_s^{-2} = 3\frac{d}{d\eta}(1 + R) = 3R' \tag{3.17}$$

Now, remembering that $\rho_b \propto a^{-3}$ and $\rho_\gamma \propto a^{-4}$ we may write $\rho_b = \rho_{b0}a^{-3}$ and likewise for ρ_γ. Since $\rho_{i0} = \Omega_i \rho_c = \Omega_i 3H_0^2/8\pi G$, we eventually reach[13]

$$R = \frac{3}{4}\frac{\rho_b}{\rho_\gamma} = \frac{3}{4}\frac{\rho_{b0}a^{-3}}{\rho_{\gamma0}a^{-4}} = \frac{3}{4}\frac{\Omega_b\rho_c}{\rho_{\gamma0}}a = \frac{3}{4}\frac{\Omega_b\frac{3H_0^2}{8\pi G}}{\frac{\pi^2}{15}T_0^4}a \approx 3\cdot10^4\cdot\Omega_b h^2 a = 3\cdot10^4\cdot\omega_b a, \quad (3.18)$$

where $\rho_{\gamma0}$ is computed from T_0, the CMB temperature today and Bose-Einstein statistics.

The fact that $R \propto a$ yields that $R' \propto a'$. Compare now the timescale of R' to the expansion time scale, namely the Hubble time:

$$\frac{(R'/R)^{-1}}{\mathcal{H}^{-1}} = \frac{(R'/R)^{-1}}{(a'/a)^{-1}} = \frac{R}{a}\frac{a'}{R'} \sim 1 \tag{3.19}$$

Thus for time scales shorter than the Hubble time we may approximate

$$c_s^{-2} \propto R = const. \tag{3.20}$$
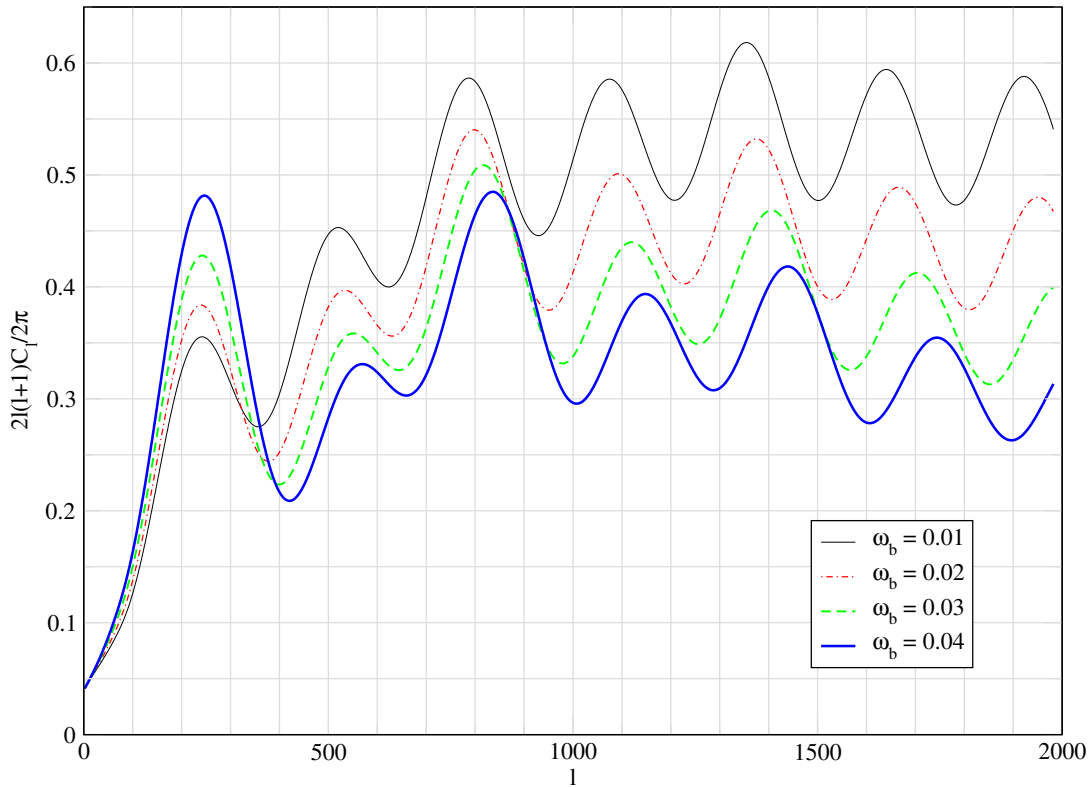
Figure 3.13:   The angular power spectrum $2\ell(\ell+1)C_\ell/2\pi$ for different baryon energy densities without the simulated diffusion damping effects. Here you can see clearly how increase in baryon density separates the odd and even peaks throughout the spectrum. For low ω_b the oscillation amplitudes alternate less. Without damping the overall power of the spectrum is lower for high baryon density. Here we have used $\Omega_m h^2 = 0.20$.

Regarding the acoustic oscillations the applicability of this approximation would require that the period of the oscillations was significantly less than the Hubble time. For qualitative discussion we apply the approximation for all scales that exhibit acoustic oscillations within the horizon, before decoupling.

The solution of equation (3.16) in the constant (Φ, Ψ, R) approximation is according to Appendix A:

$$[\Theta_0 + (1 + R)\Phi](\eta) = [\Theta_0 + (1 + R)\Phi](\eta_{\mathrm{md}})\cos(ks) \equiv A\cos(ks) \qquad (3.21)$$
$$\Leftrightarrow (\Theta_0 + \Phi)(\eta) = A\cos(ks) - R\Phi \qquad (3.22)$$

Here η_{md} denotes some conformal time in the matter-dominated era. The only time dependent variable on the right is the *sound horizon*,

$$s(\eta) \equiv \int_0^\eta c_s(\eta')d\eta'. \qquad (3.23)$$

In the $\Phi' = 0$ approximation the effective temperature oscillates around an equilibrium value that is shifted from the zero value by $-R\Phi$. Gravitational perturbation for initial overdensities is negative, so this effect amplifies the positive (odd, compressional) peaks of the spectrum and weakens the even peaks.

Note also that increasing the baryon density decreases the sound speed and therefore reduces the sound horizon which in turn increases the period of the oscillations with respect to k.

These effects are visible if two conditions are satisfied: $(\Theta_0 + \Phi) \sim R\Phi$ (for the shift of equilibrium) and $1 \sim R$ (for sound speed). The magnitude of R must be assessed from Eq. (3.18). Table 3.2 lists the decoupling values for R in different ω_b models. It tells us that R is of the order of unity near decoupling, making the change in the oscillation periods detectable. Since Θ_0 is also of the order of unity, and Φ decays effectively for large k, we do not expect to observe the equilibrium shift for small scales (large k).

ω_b	R_{dec}
0.01	0.166
0.02	0.341
0.03	0.515
0.04	0.690
0.05	0.865

Table 3.2: The baryon-photon momentum ratio in decoupling

Hu and Dodelson point out two separate effects due to baryons: they enhance the amplitude of the oscillations and shift the equilibrium of the effective temperature $(\Theta_0 + \Phi)$ to $\Theta_0 = -(1 + R)\Phi$. On account of the latter, the former has an ambiguous result: the absolute values of the positive peaks are reduced and the negative peaks are enhanced. Changes in the amplitude of the oscillations are however very subtle (Figure 3.3 offers some hint of this). However baryon density has much stronger impact on diffusion damping. This makes it very hard to detect other changes in the amplitude.

Figures 3.15 and 3.16 show the decoupling values of Θ_0 and other related variables first with and then without the added diffusion damping. In these two plots multiple

different effects conspire to produce the observed baryon effects in the oscillation amplitudes. First the increment in the oscillation amplitude, barely perceptible around the first peak (small k, large scales) is indeed the previously mentioned amplitude enhancement. The effect is due to the fact, that adding baryons to the fluid doesn't change the initial conditions. If the same initial velocity applies to a fluid with more mass it necessarily acquires more energy and thus greater oscillation amplitude. For scales smaller than the damping scale at decoupling ($k_D(\eta_{\mathrm{dec}}) \sim 300H_{100}$), the dominating effect is diffusion damping. Photon mean free path depends greatly on electron density that in turn is increased with baryon density.

It is illuminating to note, that the Equation (3.16) with the approximations ($\Phi' = 0, R' = 0, c_s' = 0$), is in direct analogy to a body of a mass $(1 + R)$ hanging on a spring in constant gravitational field. Consider a body of mass m, suspended on a spring with Hooke constant K in a gravitational field with constant gravitational acceleration g. The equation of motion is then

$$F = m\ddot{x} = -mg - Kx \quad \Leftrightarrow \quad \ddot{x} = -\frac{K}{m}(x + m\frac{g}{K}) \qquad (3.24)$$

If we rewrite the constants as $m = 1 + R = 1/3c_s^2$, $K = k^2/3$ and $g/K = \Phi$, we arrive to (3.16). Thus the mass sets the tension of the spring that has a counterpart, the sound velocity. The spring constant corresponds to the scale of the Fourier mode and the two gravitational potentials correspond as well. The left hand side of the equation is still missing the second time derivative of the gravitational potential, but in this approximation it is negligible and we could add the second derivative of the constant $(1 + R)\Phi$, to the LHS to complete the analogy with Eq. (3.16)

In our case the spring consists of the gravitation of the overdensity and the pressure of the photons. If the mass on the spring is increased, the equilibrium moves downwards. Likewise, increasing the baryon energy density (and with it R) increases the mass of the fluid: the fluid is concentrated into denser and denser regions before radiation pressure equals the two forces. If the same initial conditions lead to a larger amplitude of the first compression phase, then the energy of the oscillator must also increase. Thus the amplitude of the decompression phase can be expected to increase as well.

Let us now return to the angular power spectra in Figures 3.12-3.14. The spectra confirm that the origin of the observed effects lies in the effective temperature $(\Theta_0 + \Phi)$. The part of the line-of-sight integral that corresponds to this is

$$\int_0^\infty \frac{\mathrm{d}k}{k} \left(\Theta_0(\eta_{\mathrm{dec}}, k) + \Phi(\eta_{\mathrm{dec}}, k)\right)^2 j_\ell^2[k(\eta_0 - \eta_{\mathrm{dec}})]. \qquad (3.25)$$

Figure 3.15 shows $\Theta_0(\eta_{\mathrm{dec}}, k)$ and $\Phi(\eta_{\mathrm{dec}}, k)$ separately, summed and finally summed and squared. The cross terms between this monopole term and the dipole or ISW are insignificant, so the squared term is expected to carry the baryon peak enhancing/reducing effect to the angular power spectrum.

To clarify things further we removed the effect of damping from the decoupling values, yielding Figure 3.16. From these figures the alternating peak behavior for high baryon density models is evident. Also we can clearly observe how the change in sound speed changes the period of these oscillations.

However, the temperature curve in the topmost section of Fig. 3.16 has some intriguing characteristics that are not completely covered by our preceding discussion. Observe how the amplitude of the low baryon density curve (green) increases with k
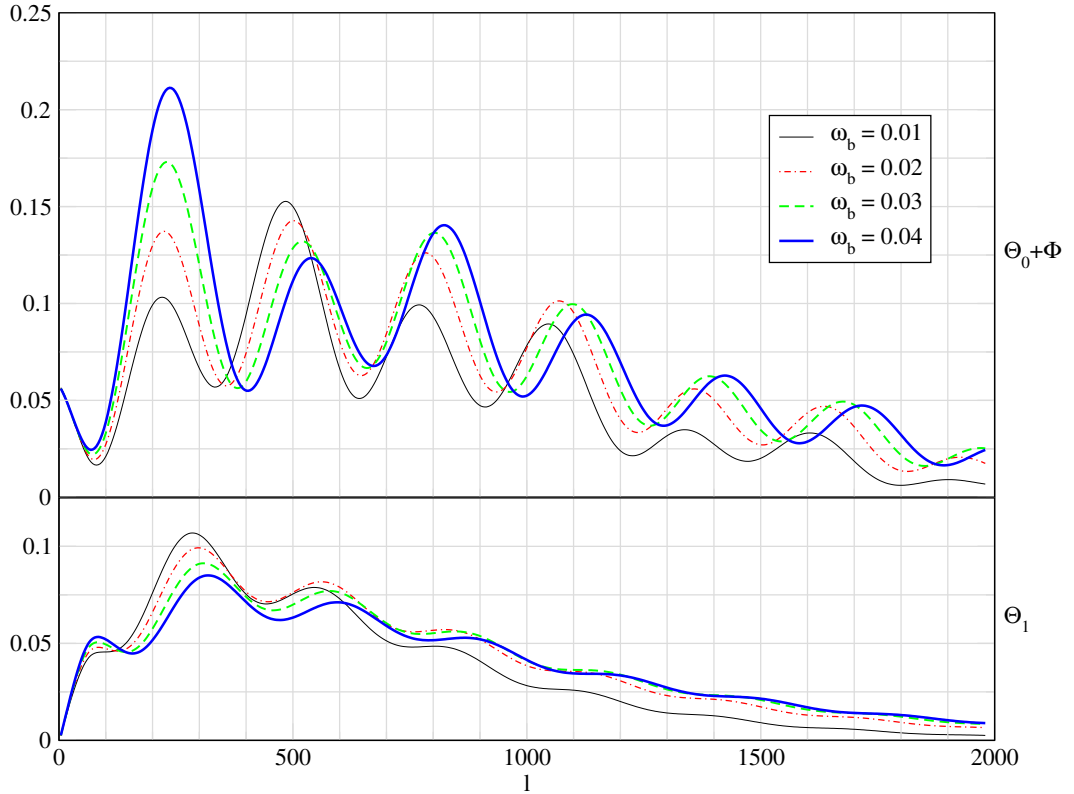
Figure 3.14: The angular power spectrum for the monopole $(\Theta_0 + \Phi)$ and dipole (Θ_1) terms. As expected, the comparison of these and Figure 3.12 shows that all the characteristic effects of baryon density increment are transmitted via the effective temperature. Here we have used $\Omega_m h^2 = 0.20$.

and outpowers higher baryon density models for small scales. This is an effect you cannot observe with diffusion damping present, since it has the opposite effect for small scales as a function of baryon density. It does serve as an example of how the energy of the oscillator is distributed in decoupling to its two components, photon and baryon fluids. See, adding baryons *increases* the energy of the oscillator, but also increases the baryons' share of the energy in decoupling. The latter effect is more significant: after decoupling the photon fluid has *less* energy, when there are more baryons present.

Figure 3.17 shows the time evolution of a single Fourier mode, $k = 400 H_{100}$. The undamped decoupling values indicate that the oscillation amplitude is strongest for models with low baryon density. However you can see from the plot that for the oscillations that occur before decoupling it is the model with highest baryon density that has the largest amplitude.

3.3.1 Sound Speed And Peak Separation

Looking at the angular power spectra of Figures 3.12-3.13 we noted that decreasing the amount of baryons seems to compress the acoustic peaks to larger angular scales to the left (smaller ℓ). Closer examination reveals that it is not the phase of the oscillations
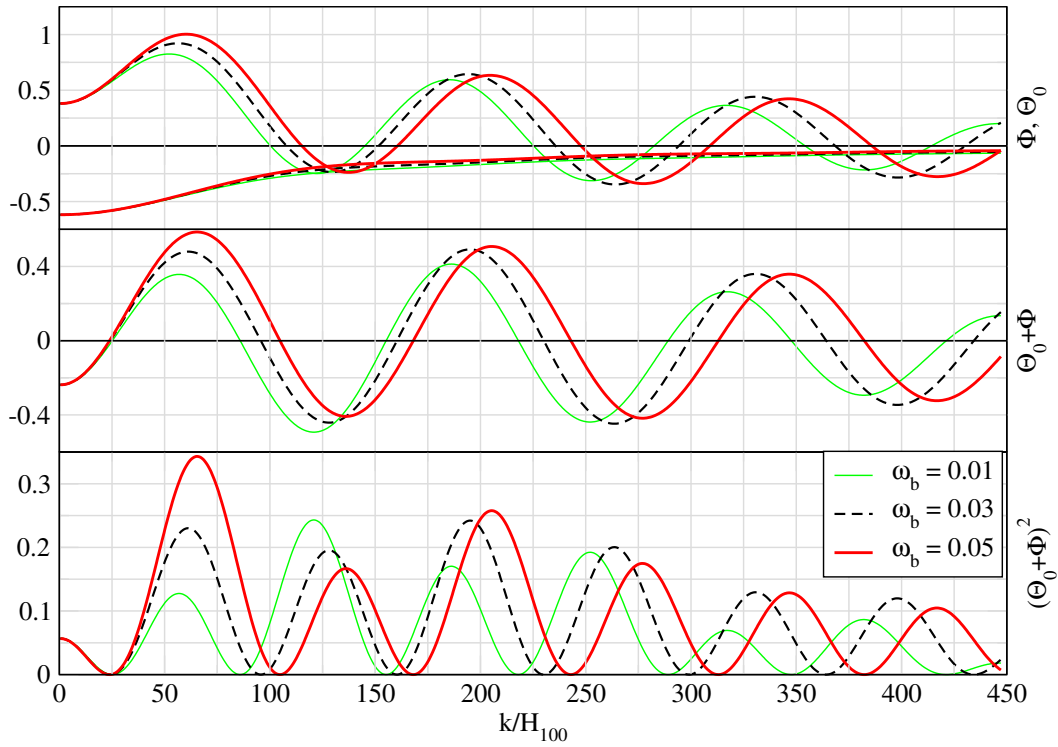
Figure 3.15: $\Theta_0(\eta_{\mathrm{dec}}, k)$ and $\Phi(\eta_{\mathrm{dec}}, k)$ separately, summed and squared for different baryon energy densities. The function in the lowest plot is integrated with the spherical Bessel function $j_\ell^2[k(\eta_0 - \eta_{\mathrm{dec}})]$ to produce the angular power spectrum in Fig. 3.11. Here we have used $\Omega_m h^2 = 0.20$.
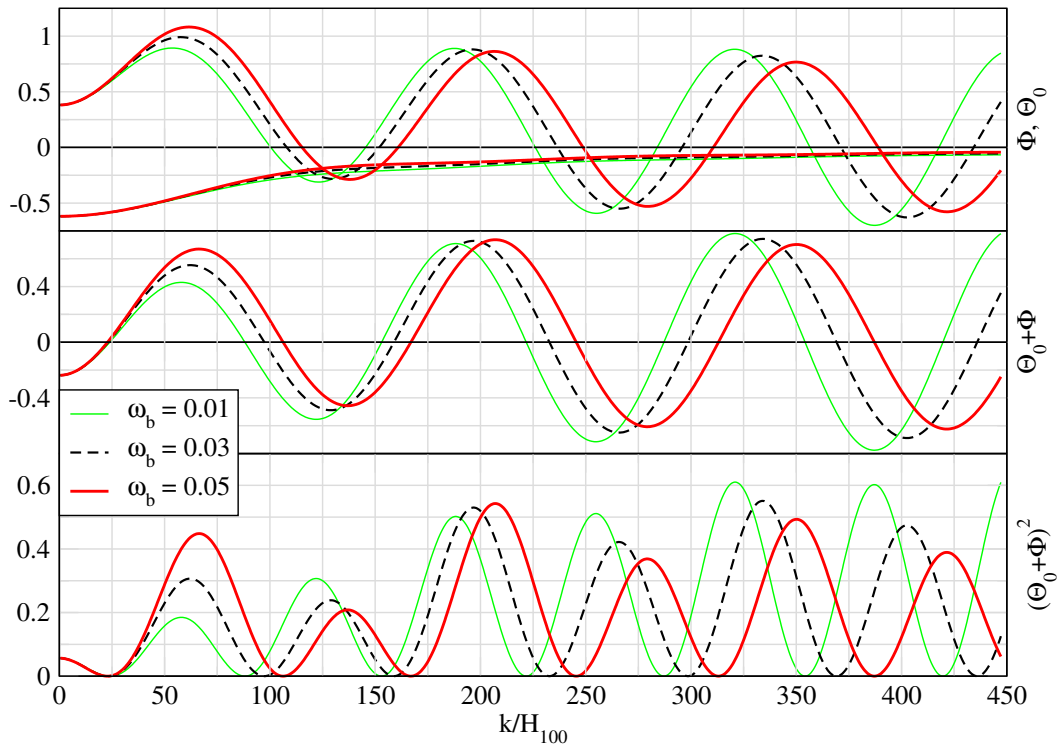

Figure 3.16: $\Theta_0(\eta_{\mathrm{dec}}, k)$ and $\Phi(\eta_{\mathrm{dec}}, k)$ separately, summed and squared for different baryon energy densities. These values were computed without the effects of damping. Now the alternating amplitude pattern is apparent for the high baryon density case. Here we have used $\Omega_m h^2 = 0.20$.
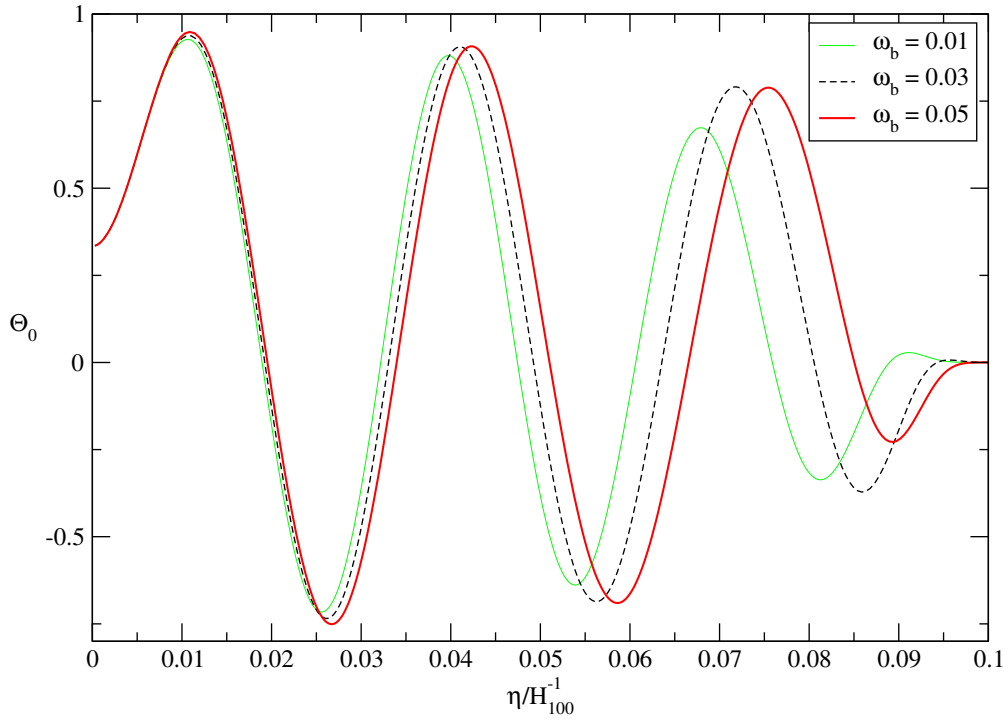
Figure 3.17: For a single Fourier mode ($k = 400H_{100}$) increasing baryon density enhances the amplitudes of both compression and rarefaction phases. It indicates that the energy of the oscillation increases. Since the decoupling amplitudes in Fig. 3.16 follow an opposite trend, it is implied that the additional energy decouples with the baryons before last scattering, leaving the photon oscillations with smaller amplitude. Here we have used $\Omega_m h^2 = 0.20$.
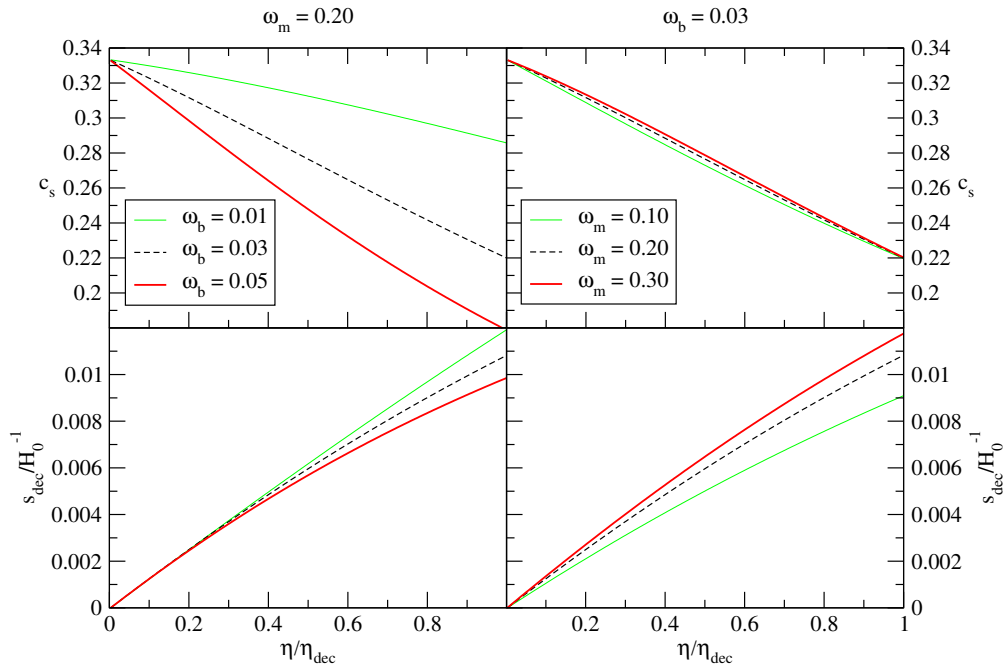
Figure 3.18: Both matter and baryon densities affect the acoustic scale that is proportional to the ratio $H_0^{-1}/s_{\rm dec}$, though the mechanism is different. Increasing baryon density slows down the speed of sound thus shortening the sound horizon. Increasing matter density reduces the Hubble length but also accelerates the expansion of the universe thus decreasing the comoving distance sound can travel before decoupling. As a net result the acoustic scale decreases.

that changes but the separation of the peaks. Customarily this separation is called the *acoustic scale*, ℓ_A.

Combining Equations (3.22) and (3.25) we can write the monopole contribution to the angular power spectrum as

$$C_\ell^{\Theta_0+\Phi} \approx \int_0^\infty \frac{\mathrm{d}k}{k} A^2 \cos^2 (ks_{\mathrm{dec}}) j_\ell^2(k\eta_0), \qquad (3.26)$$

where we have approximated $\eta_0 - \eta_{\mathrm{dec}} \approx \eta_0$ and $R\Phi \ll A$.

The first peak for the spherical Bessel function is located near $\ell = k\eta_0$ and its amplitude decreases swiftly after that. The peaks of the monopole term are located in $ks_{\mathrm{dec}} = m\pi$, where m is any integer. These peaks manifest at multipoles

$$\ell \approx k\eta_0 = m\frac{\pi}{s_{\mathrm{dec}}}\eta_0 \equiv m\ell_A. \qquad (3.27)$$

In this equation $\eta_0 - \eta_{\mathrm{dec}} \approx \eta_0$ is the comoving distance to the last scattering surface. If we considered also open and closed models it would need to be replaced by the comoving angular diameter distance. The latter is a distance concept that relates the physical size of distant objects to the angle at which they are observed. The significance of the ratio s_{dec}/η_0 is that in flat geometry it gives the angle at which the sound horizon at decoupling is viewed.

Here we have found the acoustic scale as a function of the comoving distance to the last scattering surface and the sound horizon at decoupling. The comoving distance to the scattering surface can be computed from the Friedmann equation and is in turn proportional to the Hubble length, H_0^{-1}:

$$\ell_A = \frac{\pi\eta_0}{s_{\mathrm{dec}}} \propto \frac{H_0^{-1}}{s_{\mathrm{dec}}} \qquad (3.28)$$

In our model the constant of proportionality is fixed. For more general cases with non-flat geometries or dark energy it is a function of the density parameters.

Baryons alter the acoustic scale by affecting the sound horizon. Since the sound speed is a weighted average of the two fluid components, photons and baryons, decreasing the baryon density parameter increases the sound speed and thus pushes the sound horizon further. Although this also advances decoupling (see Fig. 3.5), the latter effect is weaker. The net result is, that the ratio $H_0^{-1}/s_{\mathrm{dec}}$ decreases with the baryon density parameter and accordingly also with the acoustic scale. For the angular power spectrum this implies that the peaks appear to compress to the left.

3.4 Matter Density and the Power Spectrum

Gravitational perturbations reflect similar concentrations in the dominating energy component. These concentrations evolve due to two opposing effects: the overdense regions gather more energy through gravitation but the energy densities decrease due to expansion and pressure-driven rarefaction.

Expansion is affected by the dominating energy component. The radiation dominated universe expands faster and permits thus less growth for the initial perturbations. Also radiation has pressure, which sets a limit to the overdensity. Scales that enter the horizon during radiation domination have their gravitational potentials severely reduced by these two facts. The duration of this epoch is determined by matter and radiation densities.

One way to qualitatively approach this is to consider the matter-radiation ratio. At any given moment the matter-radiation ratio can be given in terms of the matter density parameter and the scale factor[2]. Repeating some steps of Section 3.3 we can show that:

$$\frac{\rho_m}{\rho_r} = \frac{\rho_{m0}a^{-3}}{\rho_{r0}a^{-4}} = \ldots \approx 2.4 \cdot 10^4 \cdot \omega_m a \tag{3.29}$$

For one thing this result tells us, that the expansion scale a at matter-radiation equality is inversely proportional to matter energy density, that is

$$a_{\text{eq}} \propto \frac{1}{\omega_m}. \tag{3.30}$$

This means that increasing matter energy density causes the universe to become matter dominated earlier, that is with smaller a.

The effect of matter density, ω_m, is transmitted to the spectrum with the aid of baryons. Hu and Sugiyama[12] give a notable discussion of the effect of the Hubble parameter h to the height of the acoustic peaks. We set $\Omega_m = 1$, $\omega_m = \Omega_m h^2 = h^2$, making ω_m and h equivalent parameters. Thus much of their discussion applies to our model directly. As the photon-baryon fluid oscillates through its compressions and rarefactions, the two driving forces are the gravitational perturbation and fluid pressure. Effectively the pressure is due to photons, as baryon pressure is approximated negligible.

For the total pressure perturbation we may write

$$\delta p \approx \delta p_\gamma = \frac{1}{3}\delta\rho_\gamma = \frac{1}{3}\bar{\rho}_\gamma\delta_\gamma = \frac{4}{3}\bar{\rho}_\gamma\Theta_0 \tag{3.31}$$

Recall from Section 3.3 how we wrote

$$c_s^2 = \frac{1}{3(1+R)} = \frac{\bar{\rho}_\gamma}{3(\bar{\rho}_\gamma + \frac{3}{4}\bar{\rho}_b)} \tag{3.32}$$

Combining equations (3.31) and (3.32) leads to a useful relation:

$$\delta p \approx (4\bar{\rho}_\gamma + 3\bar{\rho}_b)c_s^2\Theta_0. \tag{3.33}$$

During the positive peaks of the effective temperature, $[\Theta_0 + \Phi](\eta_{\text{dec}}, k)$, the photon-baryon fluid is at its compressional phase indicated by high pressure. The effective

---

[2]There is little point to fiddle with the radiation density. It can be computed from the CMB temperature which in turn is known to high accuracy.

temperature is lower than this, for the observed CMB photons must climb up from the potential well to reach us. This is represented by a negative Φ. In conclusion, the positive peaks correspond to compressional phases within the potential wells (or rarefaction phases outside them). The negative peaks occur as the fluid expands within the well and for photons departing the well at this time the gravitation strengthens the contrast by further cooling the escaping photons. Bear in mind this discussion as we will return to it shortly.

Fixing the baryon density parameter $\omega_b = \Omega_b h^2$ we may study the effect of total matter density on the angular power spectrum. For $\omega_b = 0.03$ the results are displayed in Figure 3.19.
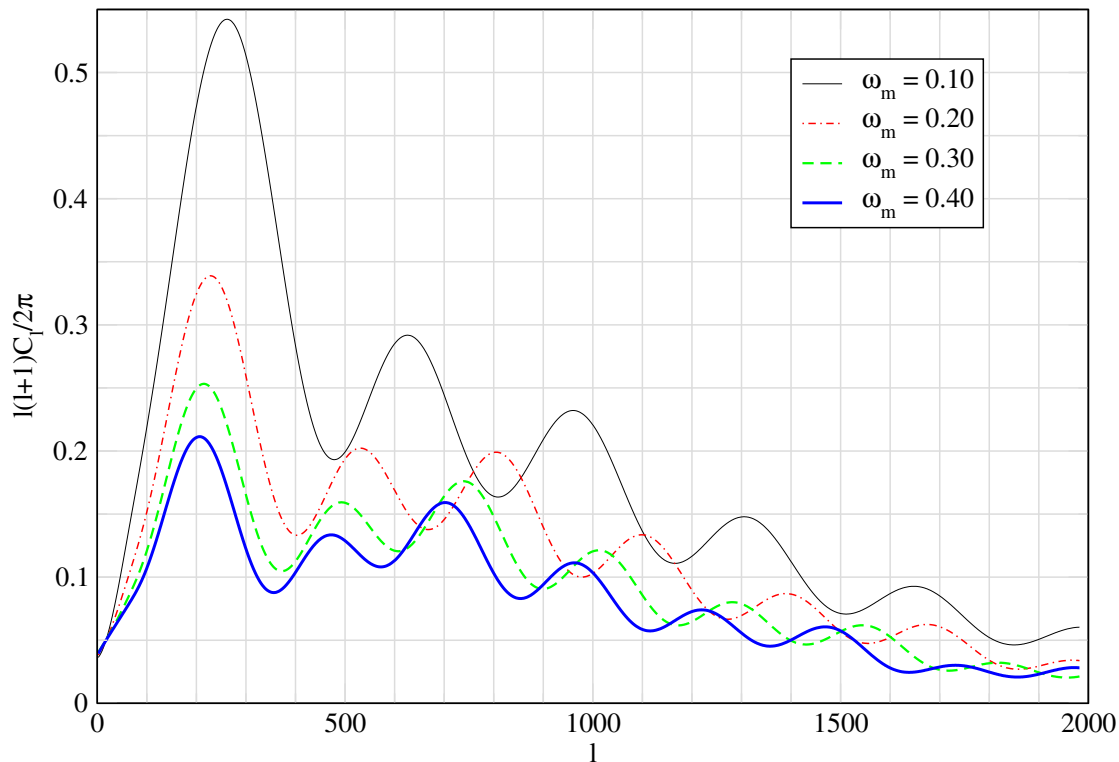

Figure 3.19: Increasing ω_m suppresses the entire spectrum. Furthermore the two first peaks decrease by a larger factor, enhancing the third and following peaks in respect to them. Finally the period of the acoustic oscillations appears to shorten as ω_m increases. Here we have used $\Omega_b h^2 = 0.03$.
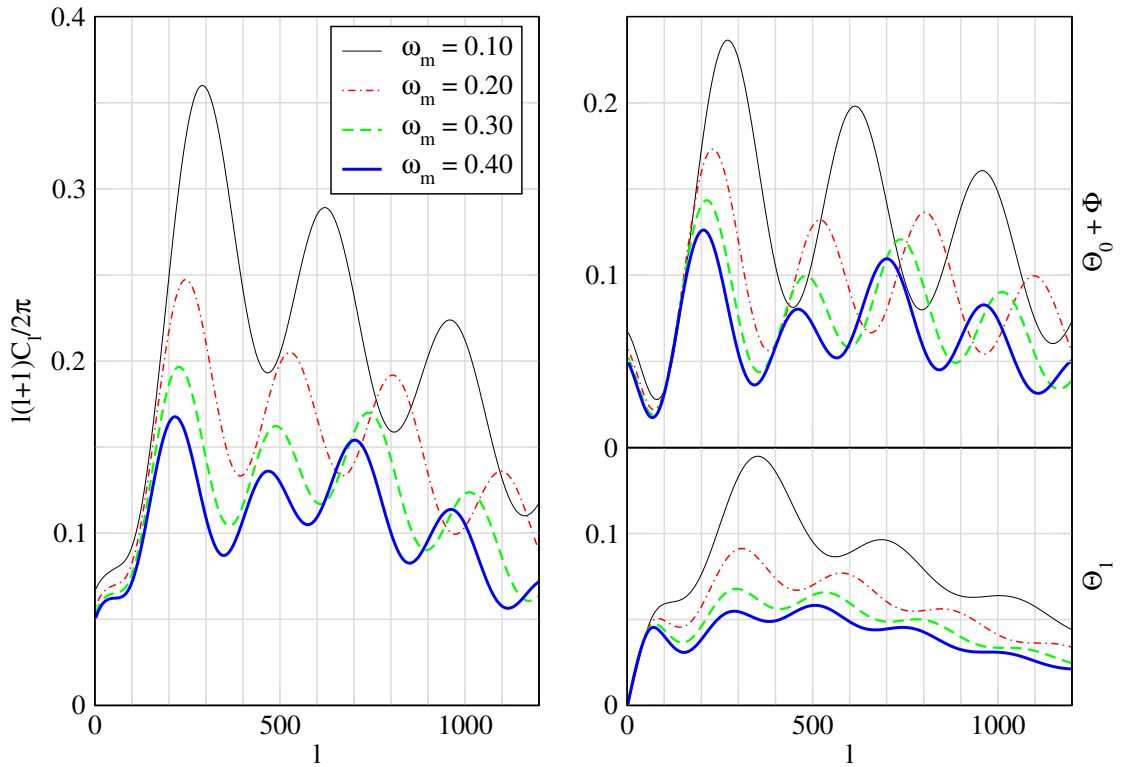
Figure 3.20: Unlike with baryons, ω_m affects the spectrum via both the effective temperature and the dipole term. Tick intervals in all three graphs are equal to ease the comparison. The first peak gains extra contribution from the cross terms of I_{SW} and the multipoles, so ISW-related terms are removed from this plot (cf. Figure 3.19 for the missing ISW). Here we have used $\Omega_b h^2 = 0.03$.

It appears that increasing the matter density does three things to the power spectrum:

- overall power of the spectrum is decreased

- the third peak grows in strength in respect to the beginning of the spectrum

- period of the oscillations shortens

As with baryons, we may well expect that effects that manifest on all scales must be transmitted by the multipole terms, not the integrated Sachs-Wolfe effect (nevertheless also the ISW is investigated in Fig. 3.25). Figure 3.20 shows that matter density has a characteristic imprint on both monopole *and* dipole power spectra.

Naturally we must trace the phenomenon back into Fourier space. Figure 3.21 shows the values of the perturbations at decoupling for Fourier modes $k = (0, 300H_{100})$ and Figure 3.22 shows the values of the perturbations at decoupling for Fourier modes in Hubble units $k \in (0, 1000H_0)$. The scaling with Hubble units in Fig. 3.22 has the advantage that the curves for different matter density models can be easily compared, since the differences in the spectra are the same as in the angular power spectrum.
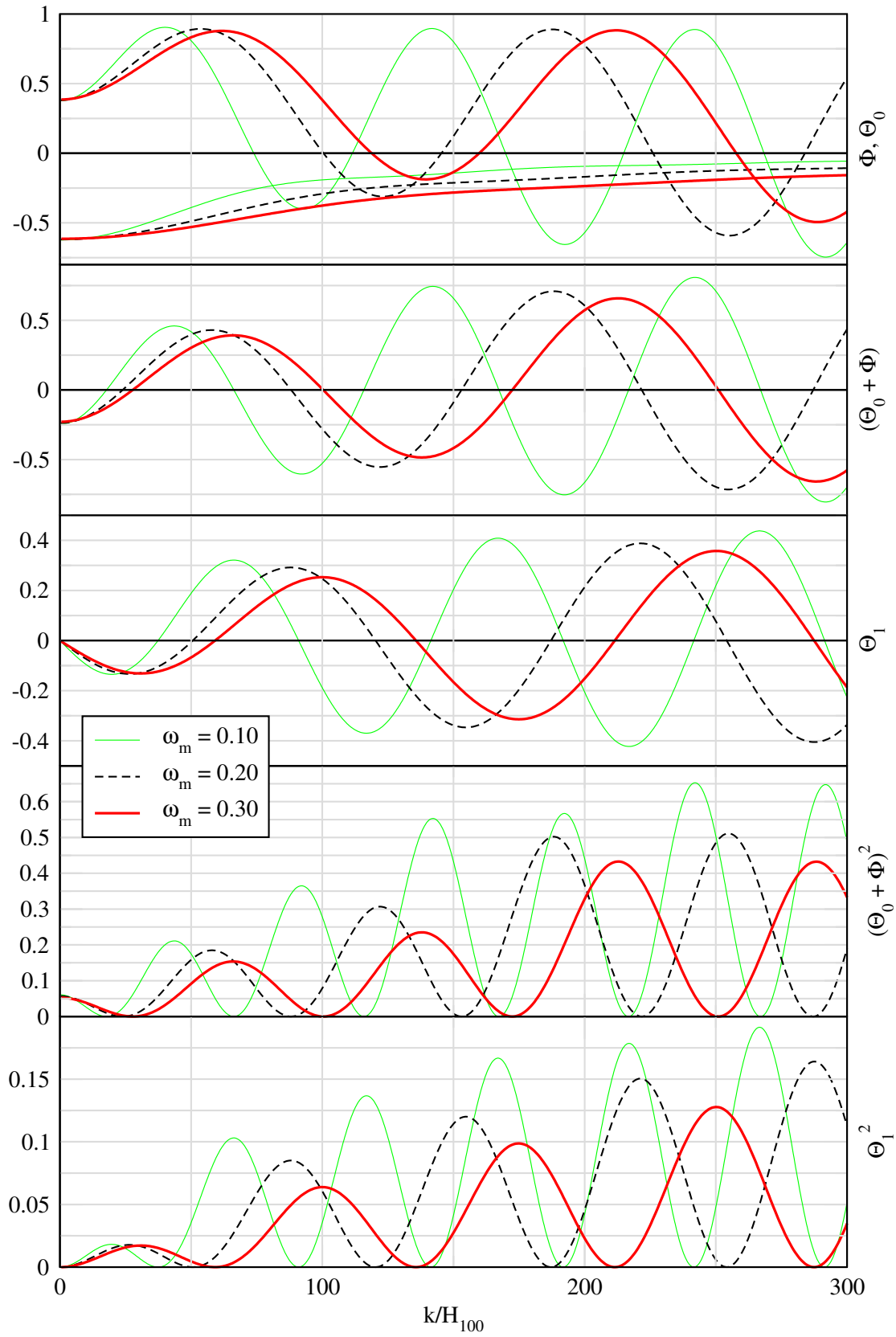
Figure 3.21:   These are the decoupling values for the gravitational potential, photon monopole and photon dipole for different Fourier modes. To separate the matter related effects we decreased baryon density to $\Omega_b h^2 = 0.01$. As you can observe, odd and even peaks behave almost equivalently. This figure does not include diffusion damping.

Figure 3.22: The decoupling values are plotted here with respect to k/H_0 and thus their relative differences in the curves reflect similar differences in the angular power spectrum. Also here baryon density is $\Omega_b h^2 = 0.01$. This figure does not include diffusion damping.

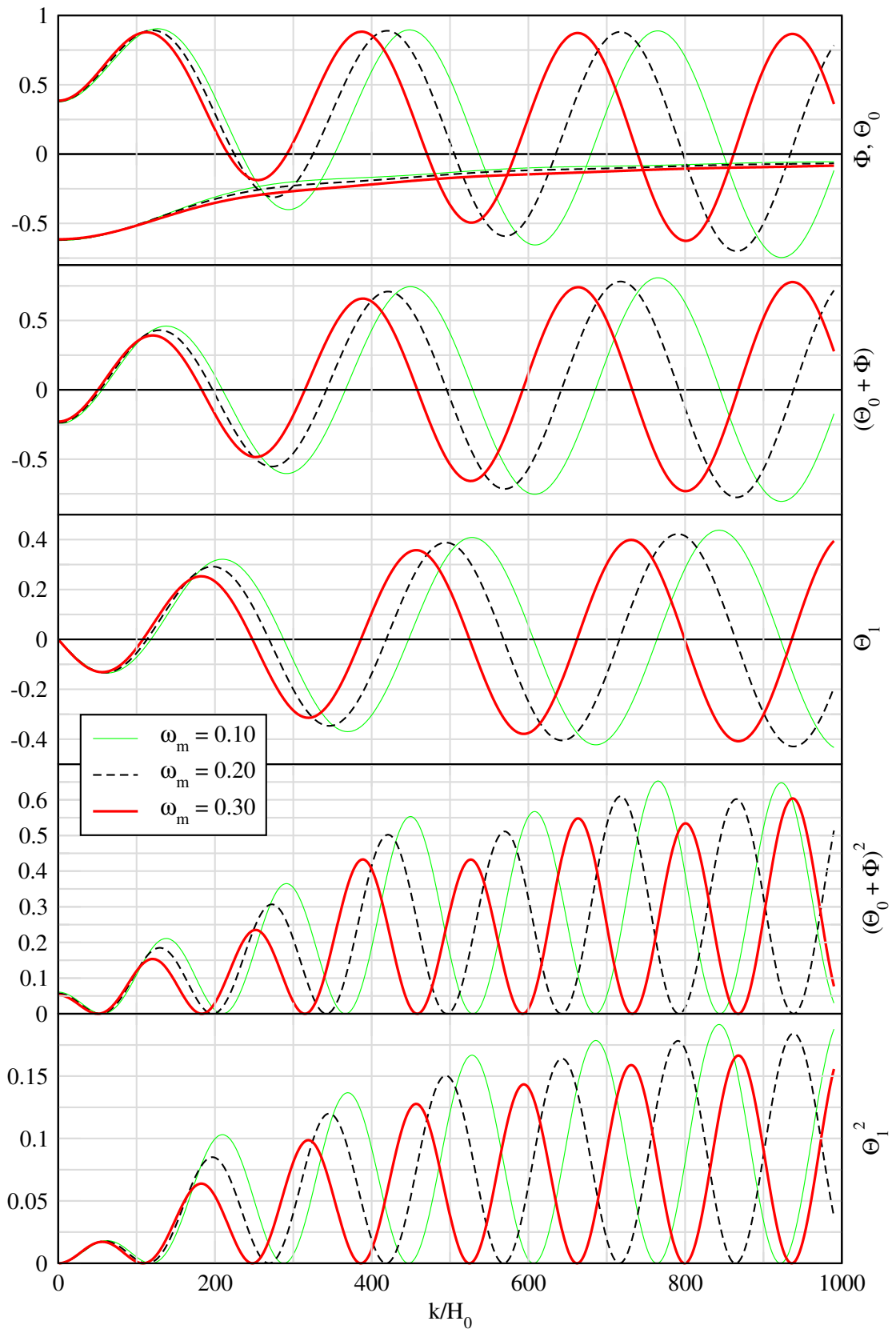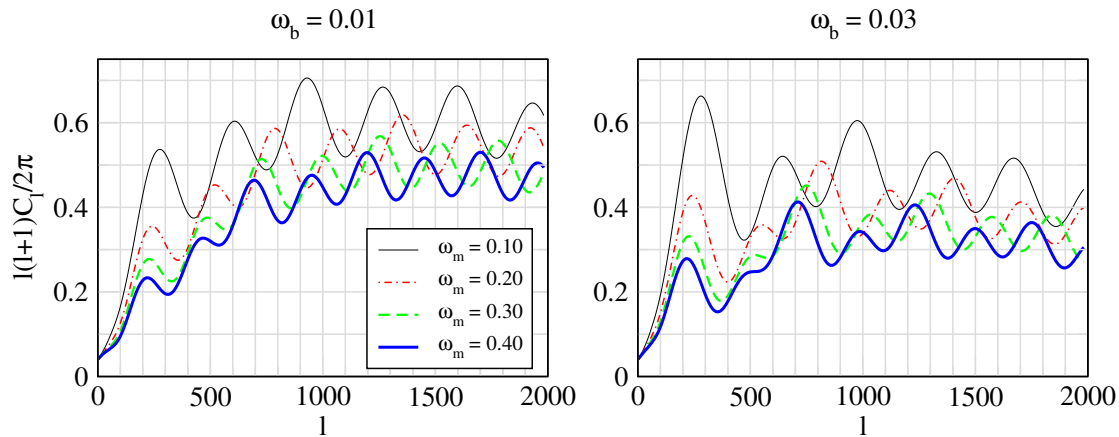Figure 3.23: The angular power spectrum for average and low baryon densities with different matter densities. To separate the matter related effects we decreased baryon density to $\Omega_b h^2 = 0.01$. As you can observe, odd and even peaks behave almost equivalently. These plots are without the simulated damping to show that the loss of power is not related to the damping scale.

3.4.1   Matter Density and the Overall Power of the Spectrum

To begin to explain what we have seen we need to discuss one more mechanism that has its impact on the structure of the acoustic peaks. Hu and Dodelson[11] refer to it as *radiation driving*.

As discussed earlier in Section 3.1, radiation dominance evens the gravitational potential for the scales that enter prior to matter-radiation equality. In the evolution plots this can be seen to occur during the first compression-rarefaction of the photon-baryon fluid (see Fig. 3.2). To keep the gravitational potential stable the fluid would need to compress, but radiation pressure instead forces it to expand. During the fluid's rarefaction the potential decays heavily. This permits the fluid to expand further.

Amplitude of the expansion is determined by the depth of the gravitational potential. How deep the well remains is determined by the matter-radiation ratio which we learned to be proportional to ω_m. Higher matter ratio implies less radiation driving effects and thus smaller amplitudes to the oscillations. Since it is the oscillations altogether, that manifest as acoustic peaks, the inhibition of radiation driving explains why the overall power of the angular power spectrum of the anisotropies is diminished.

Figure 3.24 was set up to study the dependency of radiation driving and matter density at single Fourier mode $k = 400 H_{100}$. It shows two separate, but related effects that can be combined under the title "radiation driving". As noted in the preceding, the instant of matter-radiation equality sets the final depth of the gravitational potential. This depth redshifts the departing photons that we observe in their effective temperature of the CMB. We now note, that reducing matter leads to a shallower gravitational potential and hence higher effective temperature for the oscillations. As a result the odd, compressional amplitudes grow in strength and the cooler rarefaction phases weaken, since they both suffer less cooling redshift effects.

On the behalf of the rarefactional amplitudes a competing effect is present. Since the gravitational potential decays alongside with the compressing photon-baryon fluid, the first expansion phase has less gravitation to hinder its rarefaction. Here the radiation

actually *drives* the fluid further and rarer than it would expand if more matter was present and the well was deeper. Consequently the oscillations are driven to a higher amplitude. This is the effect that dominates the amplitude of the negative peaks.

If we consider the effective temperature, $\Phi + \Theta_0$, these two effects are actually one and the same. Changing the matter density does not change the equilibrium value, only the amplitude of the oscillations. Therefore we see the amplitudes grow for all the peaks of the angular power spectrum, when matter density is decreased.
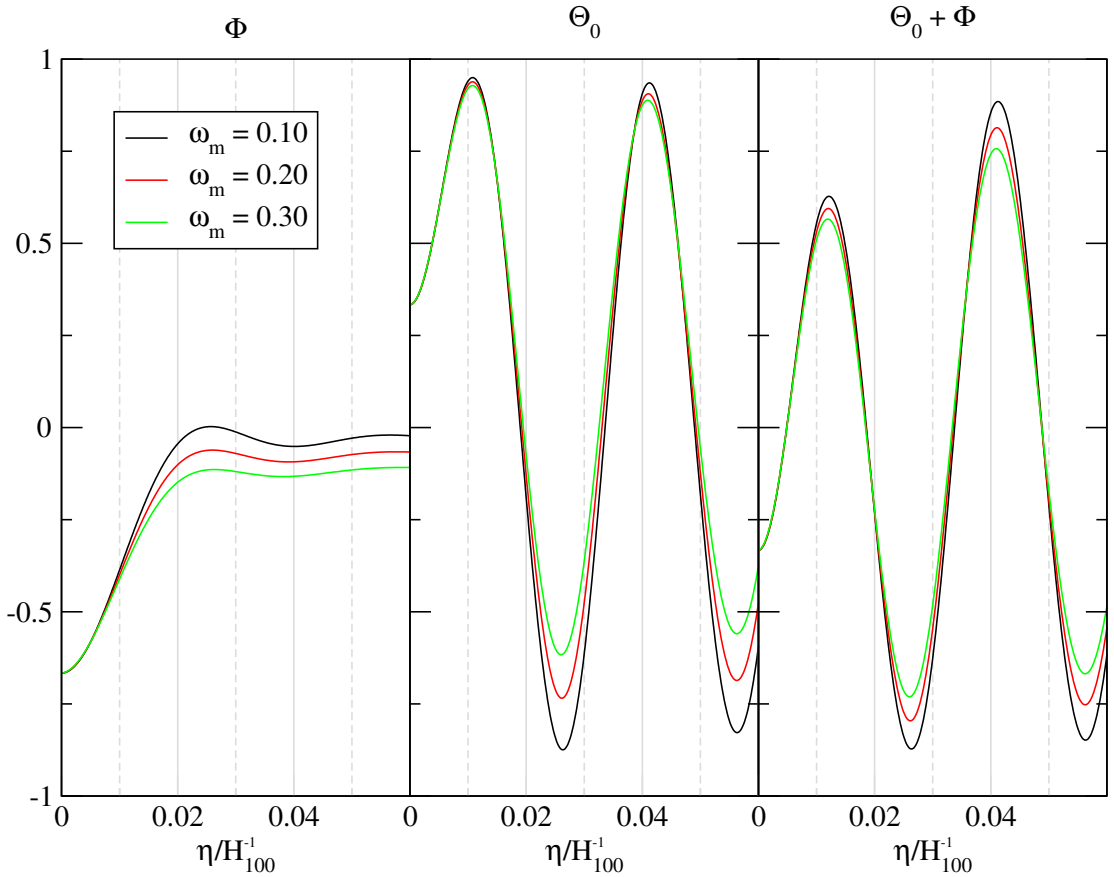
Figure 3.24: Here are the time evolutions of Φ, Θ_0, and $(\Theta_0 + \Phi)$ for $\omega_m = 0.10, 0.20, 0, 30$. The Fourier mode ($k = 400H_{100}$) enters the horizon well before matter radiation equality that occurs for these matter densities at $\eta_{\text{eq}}/H_{100}^{-1} = 0.053, 0.027, 0.018$ As ω_m decreases, there are two effects: shallowing of the gravitational potential (leftmost plot) and as a result, increment of the oscillation amplitude, also know as radiation driving (center plot). For the effective temperature (right plot) these two effects manifest in a two-way manner (see: text). Here we have used $\Omega_b h^2 = 0.03$.

3.4.2   Matter Density and the Power at Large Angular Scales

Radiation driving does not affect all of the Fourier modes. It affects only those scales that enter the sound horizon before matter domination, since no acoustic oscillation exists outside it. In their subsequent paper[13] Hu and Sugiyama showed that these effects die out quickly after the Fourier mode, k_{eq}, that enters the Hubble horizon during matter-radiation equality. It can be computed as

$$k_{eq} = \mathcal{H}_{eq} \stackrel{(2.23)}{=} \frac{4 - 2\sqrt{2}}{\eta_{eq}} \propto \omega_m. \qquad (3.34)$$

Table 3.3 shows how k_{eq} depends on matter density.

ω_m	k_{eq}/H_0	k_{eq}/H_{100}	ℓ
0.10	69.3	21.9	133
0.20	98.1	43.9	189
0.30	120.1	65.8	232
0.40	138.7	87.7	268

Table 3.3: Hubble horizon at matter-radiation equality

The angular scale ℓ that gains most contribution from Fourier mode k can be estimated by considering the C_ℓ integral, and especially the dominating monopole part:

$$\int \frac{dk}{k} ((\Theta_0(\eta_{dec}, k) + \Phi(\eta_{dec}, k)) j_\ell[k(\eta_0 - \eta_{dec})])^2 \qquad (3.35)$$

Remembering, that $j_\ell(x)$ has its first peak at $x \approx \ell$ and that its amplitude decreases steadily after that peak, we can deduct that

- Angular scales with $\ell > k_{eq}(\eta_0 - \eta_{dec})$ receive no contribution from perturbations at scale k_{eq}.

- Angular scales with $\ell < k_{eq}(\eta_0 - \eta_{dec})$ receive very little contribution from perturbations at scale k_{eq}.

For lower matter densities even the first peak can be included in the radiation driven scales. You can observe the effect of k_{eq} from Figure 3.20. For the first acoustic peak the Sachs-Wolfe effect contributes coherently and therefore it was necessary to remove the ISW part to display the k_{eq} effect.

It is not obvious, that radiation driving should boost the first acoustic peak. It corresponds to such Fourier modes that have only enough time to reach their first compression before the last scattering and thus receive no boost on their amplitude in the manner described. How does their amplitude increase then? Looking again at Figure 3.24 it shows that the amplitude of the first compression really changes relatively little in comparison with the other peaks. What does change is the depth of the gravitational well that serves as a last scattering point for the photons of the first acoustic peak. Even though the initial conditions guarantee that in all the different matter density models the first compression begins with equal energy, the gravitational potential at the compressional maximum deepens by increasing matter density.

The integrated Sachs-Wolfe effects occur due to evolution of the gravitational perturbations *after* decoupling. For many purposes it is a reasonably good approximation to set $\Phi'(\eta) = 0 \,\forall\, \eta > \eta_{\mathrm{dec}}$. Naturally this does not apply to the ISW effects. Since it is the radiation components of the cosmic fluid that cause the early effects, we should see stronger ISW for low ω_m models. Fig. 3.25 explores this phenomenon further and confirms this. The angular power of the ISW term also manifests in the cross terms of the multipoles and ISW. These actually form the better part or the observed ISW, but are less informative to view, since the cross terms are effected also by the monopole and dipole
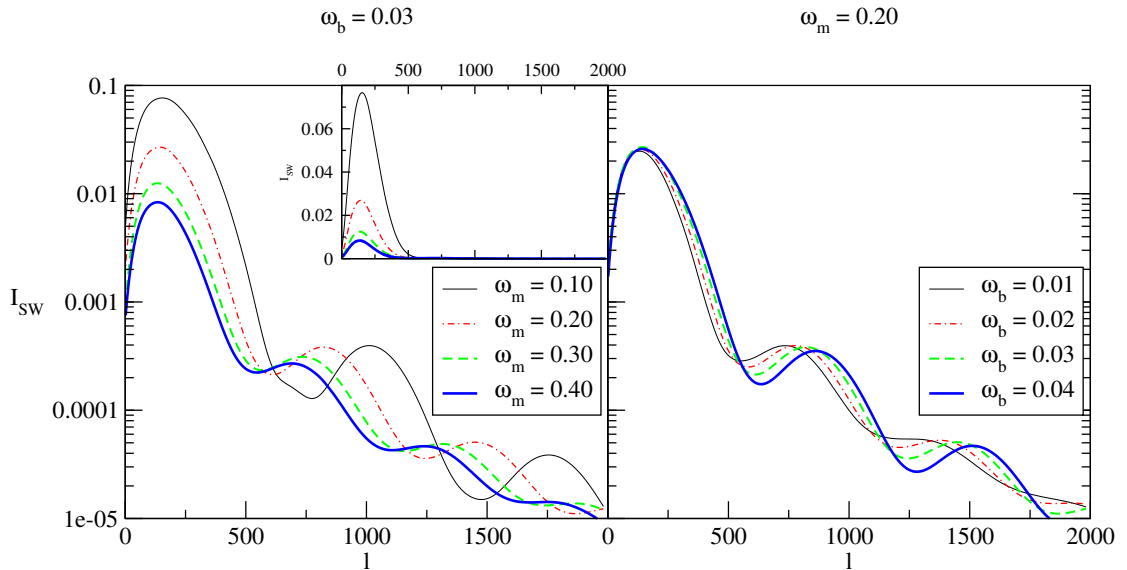

Figure 3.25: This is the angular power spectrum for the ISW effect. In the left hand plot the low matter density models have later matter domination. This extends the period of nonzero Φ' further and thus strengthens the effect. No apparent effects are detectable in the magnitude of ISW for different baryon density models.

3.4.3   Matter Density and the Peak Scale

Finally we need to address the observed change in the period of the oscillations. Increasing matter density clearly shortens the peak scale ℓ_A; the acoustic peaks are compressed left to the larger angular scales. The same can be observed for the decoupling values in Figure 3.22 when they are plotted as a function of the relative Fourier mode $k/H_0(\omega_m)$. As a function of the absolute Fourier mode the oscillation period actually increases with ω_m (cf. Fig. 3.21), but that is only related to the changes in the Hubble parameter.

In Equation (3.28) we presented a relation between the Hubble length, sound horizon and the acoustic scale:

$$\ell_A \propto \frac{H_0^{-1}}{s_{\text{dec}}} \tag{3.36}$$

Due to our parametrization, changing the matter density parameter affects both H_0 and s_{dec}. Regarding the Hubble parameter we had

$$\omega_m = \Omega_m h^2 \stackrel{\Omega_m=1}{=} h^2 \quad \Rightarrow \quad H_0 = h H_{100} \propto \sqrt{\omega_m}. \tag{3.37}$$

Now with the sound horizon the matter is more complex. Matter density affects the matter-radiation equality and the decoupling. It does not alter sound speed directly, but since it changes the expansion law, the comoving distance the sound can travel (i.e. the sound horizon) is affected.

The Friedmann equation for a flat universe,

$$\left(\frac{\dot{a}}{a}\right)^2 = \frac{8\pi G}{3}(\rho_\gamma + \rho_m), \tag{3.38}$$

indicates that the universe expands and contracts faster when there is more matter present. Figure 3.6 showed that regardless of the matter density, baryons and photons decouple at the same redshift and scale factor. If the universe does expand faster, it will reach this preset value of the scale factor earlier allowing less time for sound to travel before decoupling. As a result the sound horizon shrinks when the matter density parameter is increased.

Since both the Hubble length and the sound horizon shrink by increasing the matter density, the preceding discussion does not reveal whether the acoustic scale should grow or be reduced by increasing the matter density. Exact expression for the sound horizon at decoupling ($s_{\text{dec}}(\omega_m)$) can be computed using the background equations. However we have already computed the solution numerically for Fig. 3.18. It indicates that *when the matter density parameter is increased, the sound horizon shrinks by a smaller factor than the Hubble length.* Thus the ratio H_0^{-1}/s_{dec} decreases, as does the acoustic scale. For the angular power spectrum this means that the peaks are compressed to the left.

Chapter 4

Conclusions

Following the discussion in [5] we studied a simplified model of the universe by making a number of approximations preserving the major features of pre-recombination dynamics. We:

- omitted dark energy and as a result had no late ISW

- approximated baryonic matter by hydrogen

- ignored shear stress and assumed perfect fluid dynamics

- studied only scalar perturbations and thus neglected possible gravitational waves

- neglected reionization

- truncated the Boltzmann hierarchy to the dipole term, but applied an approximate calculation to obtain the damping scale induced by the higher multipoles

- ignored polarization dependency in the Thomson scattering

- approximated the thickness of the last scattering surface by a δ-function, except for the diffusion damping scale

These steps yielded a relatively simple model in which to study the effects of two selected cosmological parameters, ω_m and ω_b. Qualitative comparison of our angular power spectra and the results of the "CAMB" code[19] show that we were able to reproduce the key effects of the two cosmological parameters.

Having inserted the diffusion damping into the equations by hand provided us with the option to remove damping when we so choose. This proved to be a valuable tool in separation of the different effects.

The harvest of this work is not so much the already recognized behavior of $C_\ell(\omega_m, \omega_b)$, as the way these effects can be viewed through the deterministic time evolution of the cosmological perturbations before the decoupling. The oscillating photon-baryon fluid, within a framework of an expanding, CDM universe, is an exciting dynamical system with rich interactions. The effects of changes in a single parameter manifest in multiple levels.

Let us sum up the key features of these dynamics. The energy of the acoustic oscillations increases with the baryon density. This can be understood as adding more mass to an oscillator without changing its initial motion. Increased energy spells higher

oscillation amplitudes. Adding more mass to an oscillator in a gravitational well also shifts its equilibrium. The more massive oscillator is able to contract further against the fluid pressure before the rarefaction begins. Expansion of this oscillator is left short due to the additional mass and thus the equilibrium of the oscillations moves deeper into the gravitational potential. The implications of this baryon drag on the angular power spectrum are well known: odd peaks gain in strength in respect to the even peaks.

Odd peaks of the angular power spectrum correspond to fluid contractions within gravitational wells or rarefactions outside them. These motions are aided by gravitation once the mass of the oscillator increases. The even peaks on the other hand correspond to rarefactions within gravitational wells and compressions outside them. Both motions are opposed by the gravitation and thus adding mass weakens them.

Photon diffusion that evens the perturbations is affected by baryon density. This is so because the diffusion is generated by the random walks of the photons, that are characterized by the mean free path $\lambda_\gamma = 1/an_e\sigma_T$. Less baryons (and electrons) leads to longer diffusion lengths and larger damping scales: diffusion damping is hindered by higher baryon density.

Matter density determines the length of the radiation dominated era. The most profound effect that the radiation has over the perturbations is the decay of the gravitational perturbation. This occurs because the radiation component is unable to contract beyond a limit set by its pressure and because the universe's expansion exceeds the energy density build up caused by gravitational concentration. Adding matter makes the equality occur earlier thus leaving the gravitational potential stronger.

For all scales that exhibit acoustic oscillations before decoupling, the gravitational potential decays through the first compression, all the way to the first rarefaction. The amplitude of the decompression is determined by the remaining potential, whose depth is a function of the matter density. Less matter leads to later equality and more decay, thus also to a higher amplitude of the first expansion as the weaker gravitational potential resists the expansion less. The decompression phase is said to be radiation driven. The decompression also sets the amplitude of the oscillations, Therefore changes in the radiation driving affect the overall power of the spectrum. More matter, less radiation driving and correspondingly less power.

Aside from the loss of overall power, delaying the end of radiation domination has a clear impact on the low-ℓ part of the power spectrum. It allows larger scales to enter the horizon during radiation domination and be boosted by radiation driving. The scales in question reside in the vicinity of the first acoustic peak. Also the early integrated Sachs-Wolfe effect changes. With matter-radiation equality occurring later, the decay of the gravitational potentials goes on further beyond the decoupling, allowing for stronger ISW effects that also contribute coherently to the height of the first peak. Adding matter will reverse these effects and reduce the power for the beginning of the angular power spectrum.

Finally the sound horizon at decoupling sets the acoustic scale of the angular power spectrum. Both baryons and cold dark matter affect this distance, though in very different ways. Baryon density slows down the pure radiation sound speed of the photon component in the photon-baryon fluid. Higher baryon density implies thus a shorter sound horizon. This enlarges the angular scale, moving the acoustic peaks to the right in the angular power spectrum. Adding matter has the opposite effect, though sound speed is not affected. Matter speeds up the expansion of the universe and thus reduces the comoving distance the sound can travel prior to recombination. However in our

parametrization the Hubble length is also decreased and as a result the acoustic scale decreases.

Appendix A

Oscillator Equation for Photon-Baryon Fluid

In the tight coupling regime, rapid Thomson scattering maintains photons and baryons in equilibrium. This can be seen as a high collision rate:

$$|\tau'| = a n_e \sigma_T \gg 1 \tag{A.1}$$

During this epoch the baryon-photon momentum ratio $R = 3\rho_b/4\rho_\gamma \ll 1$. This holds well beyond matter-radiation equality.

For the evolution equations of temperature and baryons,

$$\Theta_0' + k\Theta_1 = \Psi' \tag{A.2}$$

$$\Theta_1' - \frac{k}{3}\Theta_0 = \frac{k}{3}\Phi + \tau'\left(\Theta_1 - \frac{1}{3}v_b\right) \tag{A.3}$$

$$v_b' + \mathcal{H}v_b = k\Phi - \frac{\tau'}{R}\left(3\Theta_1 - v_b\right), \tag{A.4}$$

this means that the collision terms dominate.

To the zeroth order, equation (A.4) reads $3\Theta_1 = v_b$. It can be differentiated to give

$$3\Theta_1' = v_b' \tag{A.5}$$

Solving first v_b from the RHS of (A.4) we may insert the zeroth order approximations and reach a first order iterated equation

$$v_b = 3\Theta_1 + \frac{R}{\tau'}\left(3\Theta_1' + 3\mathcal{H}\Theta_1 - k\Phi\right). \tag{A.6}$$

The iteration approach was first presented by Peebles and Yu[24] in 1970.

The expression for v_b can in turn be substituted in (A.3) to rid the photon equations of the baryon variables:

$$(1+R)\Theta_1' - \frac{k}{3}\Theta_0 = \frac{k}{3}(1+R)\Phi - R\mathcal{H}\Theta_1 \tag{A.7}$$

To eliminate Θ_1 we differentiate (A.2) and substitute Θ_1' from (A.7). Note that from (A.2) follows also an expression for Θ_1. These steps result in

$$\Theta_0'' + k\left[\frac{k}{3(1+R)}\Theta_0 + \frac{k}{3}\Phi + \frac{R}{1+R}\mathcal{H}\frac{1}{k}(\Theta_0' - \Psi')\right] = \Psi'' \tag{A.8}$$

The sound speed in the coupled photon baryon fluid is a weighted average of the separate photon and baryon sound speeds:

$$c_s^2 = \frac{1}{3(1+R)} \tag{A.9}$$

Since $\rho_b \propto a^{-3}$ and $\rho_\gamma \propto a^{-4}$, is $R \propto a$ and thus

$$\frac{1}{R}\frac{\mathrm{d}R}{\mathrm{d}\eta} = \frac{1}{a}\frac{\mathrm{d}a}{\mathrm{d}\eta} = \mathcal{H} \tag{A.10}$$

Making these substitutions yields

$$\Theta_0'' - \Psi'' + 3c_s^2 R'(\Theta_0' - \Psi') = -c_s^2 k^2[\Theta_0 + (1+R)\Phi] \tag{A.11}$$

Finally, noting that

$$\frac{\mathrm{d}}{\mathrm{d}\eta} c_s^{-2} = 3\frac{\mathrm{d}}{\mathrm{d}\eta}(1+R) = 3R' \tag{A.12}$$

allows us to write

$$c_s^2 \frac{\mathrm{d}}{\mathrm{d}\eta}\left[c_s^{-2}(\Theta_0' - \Psi')\right] = -c_s^2 k^2[\Theta_0 + (1+R)\Phi], \tag{A.13}$$

or

$$c_s^2 \frac{\mathrm{d}}{\mathrm{d}\eta}\left(c_s^{-2}\Theta_0'\right) + c_s^2 k^2\Theta_0 = -\frac{k^2}{3}\Phi + c_s^2 \frac{d}{d\eta}\left(c_s^{-2}\Psi'\right) \tag{A.14}$$

In a matter dominated universe the gravitational perturbations cease to evolve, i.e. $\Phi' = \Psi' = 0$. If we also ignore the evolution of

$$R \propto a \overset{\mathrm{md}}{\propto} \eta^2 \tag{A.15}$$

in $c_s^{-2} = 3(1+R)$, approximating sound speed as a constant, we may arrange (A.13) by adding $\frac{\mathrm{d}^2}{\mathrm{d}\eta^2}[(1+R)\Phi] = 0$ to the left hand side to read

$$\frac{d^2}{d\eta^2}[(\Theta_0 + (1+R)\Phi)] + c_s^2 k^2[\Theta_0 + (1+R)\Phi] = 0, \tag{A.16}$$

a simple harmonic oscillator equation for the quantity $\Theta_0 + (1+R)\Phi$. Do note that (A.13) can be solved[12] for a time dependent R, but the complexity of the solution manages to hide the underlying physics.

For the constant (Φ, Ψ, R) case the solution,

$$[\Theta_0 + (1+R)\Phi](\eta) = [\Theta_0 + (1+R)\Phi](\eta_{\mathrm{md}})\cos ks \tag{A.17}$$

tell us that the effective temperature $\Theta_0 + \Phi$ oscillates around an equilibrium point that is shifted by $-R\Phi$. Here we have used the *sound horizon*: $c_s\eta \approx s \equiv \int^\eta \mathrm{d}\eta' c_s(\eta')$, the comoving distance sound can travel in cosmological time scales.

Bibliography

[1] Bardeen, J.M., *Gauge-invariant cosmological perturbations*, Phys. Rev. D **22** 8 (1980) 1882.

[2] Bennet, C.L. et al., *First Year Wilkinson Microwave Anisotropy Probe (WMAP) Observations: Preliminary Maps and Basic Results*, ApJ Suppl. **148** (2003) 1.

[3] Davis, M., Efstathiou, G., Frenk, C.S. and White, S.D,M., *The Evolution of Large-Scale Structure in a Universe Dominated by Cold Dark Matter* ApJ **292** (1985) 371.

[4] Dicke, R.H, Peebles, P.J.E., Roll, P.G. and Wilkinson D.T., *Cosmic Black-Body Radiation*, ApJ **142** (1965) 414.

[5] Dodelson, S., *Modern Cosmology*, (Academic Press, 2003)

[6] European Space Agency (ESA) and the Planck Science Team, Planck Home Page at `http://www.esa.int/science/planck` , Planck Science Team at `http://www.rssd.esa.int/index.php?project=PLANCK&page=index` (referenced 23 Oct. 2005)

[7] Flannery, B.P., Press, W.H. and Teukolsky, S.A., *Numerical Recipes in C: The Art of Scientific Computing*, (Cambridge University Press, 1992)

[8] Galassi et al., *GNU Scientific Library - Reference Manual, Edition 1.6 for GSL version 1.6*, (2004), available online at `http://www.gnu.org/software/gsl/manual/` (referenced 23 Oct. 2005)

[9] Guth, A.H., *The Inflationary Universe: a Possible Solution to the Horizon and Flatness Problems*, Phys. Rev. D **23** (1981) 347.

[10] Hinshaw, G. et al., *First Year Wilkinson Microwave Anisotropy Probe (WMAP) Observations: Angular Power Spectrum*, ApJ Suppl. **148** (2003) 135.

[11] Hu, W. and Dodelson, S., *Cosmic Microwave Background Anisotropies*, Annu. Rev. Astron. Astrophys. **40** (2002) 171.

[12] Hu, W. and Sugiyama, N., *Anisotropies in the Cosmic Microwave Background: an Analytic Approach*, ApJ **444** (1995) 489.

[13] Hu, W. and Sugiyama, N., *Small Scale Cosmological perturbations: an Analytic Approach*, ApJ **471** (1996) 542.

[14] Hubble, E., *A Relation Between Distance and Radial Velocity Among Extra-Galactic Nebulae*, Proc. N. A. S **15** (1929) 168.

[15] Kurki-Suonio, H., *Cosmology I and II*, unpublished lecture notes partly available online at `http://theory.physics.helsinki.fi/~cosmology/` (referenced 23 Oct. 2005)

[16] Kurki-Suonio, H., *CMB Physics*, unpublished lecture notes available online at `http://theory.physics.helsinki.fi/~cmb/` (referenced 23 Oct. 2005)

[17] Kurki-Suonio, H., *Cosmological Perturbation Theory*, unpublished lecture notes available online at `http://theory.physics.helsinki.fi/~cmb/` (referenced 23 Oct. 2005)

[18] Kurki-Suonio, H., Muhonen, V. and Väliviita, J., *Correlated Primordial Perturbations in Light of CMB and LSS Data*, Phys. Rev. D **71** (2005)

[19] Lewis, A. and Challinor, A., *Code for Anisotropies in the Microwave Background*, Fortran 90 code available online at `http://camb.info` (referenced 23 Oct. 2005)

[20] Liddle, A.R. and Lyth, D.H., *Cosmological Inflation and Large-Scale Structure*, (Cambridge University Press, 2000).

[21] Ma, C.P. and Bertschinger, E., *Cosmological Perturbation Theory in the Synchronous and Conformal Newtonian Gauges*, ApJ **455** (1995) 7.

[22] Mukhanov, V.F., Feldman, H.A. and Brandenberger, R.H., *Theory of Cosmological Perturbations*, Phys. Rept. **215** (1992) 203.

[23] Peebles, P.J.E., *Recombination of the Primeval Plasma*, ApJ **153** (1968) 1.

[24] Peebles, P.J.E. and Yu, J.T., *Primeval Adiabatic Perturbation in an Expanding Universe*, ApJ **162** (1970) 815.

[25] Penzias, A.A. and Wilson, R.W., *A Measurement of Excess Antenna Temperature at 4080 Mc/s*, ApJ **142** (1965) 419.

[26] Sachs, R.K. and Wolfe, A.M., *Perturbations of a Cosmological Model and Angular Variations of the Microwave Background*, ApJ **147** (1967) 73.

[27] Seljak, U. and Zaldarriaga, M., *A Line-of-Sight Integration Approach to Cosmic Microwave Background Anisotropies*, ApJ **469** (1996) 437.

[28] Seljak, U. and Zaldarriaga, M., *CMBFAST*, available online at `http://cmbfast.org` (referenced 23 Oct. 2005)

[29] Silk, J., *Cosmic Black-Body Radiation and Galaxy Formation*, ApJ **151** (1968) 459.

[30] Smoot, G.F. et al., *Structure in the COBE Differential Microwave Radiometer First-Year Maps*, ApJ **396** (1992) L1.

[31] Spergel, D.N. et al. (WMAP Collaboration), *First Year Wilkinson Microwave Anisotropy Probe (WMAP) Observations: Determination of Cosmological Parameters*, Astrophys. J. Suppl. **148** (2003) 175.

[32] Tegmark, M. et al., *Cosmological parameters from SDSS and WMAP*, Phys. Rev.
     D **69** (2004) 103501.

[33] Väliviita, J., *The Nature of Primordial Perturbations in the Light of
     CMB Observations*, Ph.D. Thesis, (Helsinki, 2005), available online at
     `http://ethesis.helsinki.fi`.